Helsinki Institute of Physics Internal Report Series

HIP-2016-01

Numerical simulations of semiconductor radiation detectors for high-energy physics and spectroscopy applications

Timo Peltola

Division of Particle Physics and Astrophysics
Department of Physics
Faculty of Science
University of Helsinki
and
Helsinki Institute of Physics
Helsinki, Finland

Academic Dissertation

To be presented for public criticism, with the permission of the Faculty of Science of the University of Helsinki, in the auditorium A129 of the Chemicum building, A. I. Virtasen aukio 1, on Friday, March 11$^{\text{th}}$, 2016, at 12:00 o'clock.

Helsinki 2016

Supervisor:

Prof. Paula Eerola, Ph.D.
Department of Physics
University of Helsinki
Finland

Reviewers:

Dr. Ulrich Parzefall
Physikalisches Institut
University of Freiburg
Germany

Prof. Hele Savin
Department of Micro- and Nanosciences
Aalto University
Finland

Opponent:

Prof. Zheng Li, Ph.D.
Department of Physics
Xiangtan Technical University
China

Internal Report Series HIP-2016-01
ISSN 1455-0563
ISBN 978-951-51-1263-7 (printed version)
ISBN 978-951-51-1264-4 (electronic version)
`http://ethesis.helsinki.fi`
Unigrafia

Helsinki 2016

To Taru,
Light of my life
and Living Proof that
there is also magick in life

Abstract

Mainly due to their outstanding performance the position sensitive silicon detectors are widely used in the tracking systems of High Energy Physics (HEP) experiments such as the ALICE, ATLAS, CMS and LHCb at LHC, the world's largest particle physics accelerator at CERN. The foreseen upgrade of the LHC to its high luminosity (HL) phase (HL-LHC scheduled for 2023), will enable the use of maximal physics potential of the facility. However, after 10 years of operation the expected fluence will result in a radiation environment that is beyond the capacity of the present tracking system design. The required upgrade of the all-silicon central trackers will include higher granularity and radiation hard sensors that can tolerate the increased occupancy and the higher radiation levels. The radiation hardness of the new sensors must be roughly of an order of magnitude higher than in the current LHC detectors. To address this, extensive measurements and simulation studies have been performed to investigate different designs and materials for silicon sensors with sufficient radiation tolerance. The work presented in this thesis has been carried out within the frameworks of the CMS Tracker Upgrade Project and the multi-experiment RD50 Collaboration. Also an overview of the recent results within the RD50 from both measurements and simulations of several detector technologies and silicon materials at radiation levels expected for HL-LHC is provided in this thesis.

Supplementing measurements, simulations serve a vital role for e.g. device structure optimization and predicting the electric fields and trapping in the silicon sensors. The main objective of device simulations in the CMS Tracker Upgrade and RD50 is by using professional software to develop an approach to both model and predict the performance of the irradiated silicon detectors. The first quantitative models for radiation damage, based on two effective midgap levels, are able to reproduce the experimentally observed detector characteristics such as leakage current, full depletion voltage and Charge Collection Efficiency (CCE). Recent implementations of additional traps at the SiO_2/Si interface or close to it have expanded the scope of the experimentally valid simulations to surface properties such as the interstrip resistance and capacitance as well as the position dependence of CCE (CCE(x)) of strip sensors irradiated to HL-LHC fluences.

In the course of this thesis, experimental data is used to develop an effective non-uniform defect model with the Sentaurus TCAD simulation framework. Complementing the earlier proton bulk damage model, the model reproduces both the observed bulk and the surface properties and can predict the performance of strip detectors with

specific geometry in the fluence range 3×10^{14} $n_{eq}cm^{-2}$ – 1.4×10^{15} $n_{eq}cm^{-2}$. When applied to CCE(x) measurements at varying fluences, the model can provide a means for the parametrization of the accumulation of oxide charge at the SiO_2/Si interface as a function of irradiation dose.

TCAD simulations are also applied for a comparative study of a thin p-on-p pixel sensor and a more conventional p-on-n pixel sensor with similar configuration. The simulations are used to provide an explanation to the measured charge collection behaviour and for a detailed investigation of the electrical properties of the two sensor types. No previous studies of the p-on-p configuration have been conducted in the HEP community.

Finally, the scope of TCAD simulations presented in this thesis is extended to a compound semiconductor material, namely GaAs. By implementing the observed deep donor defect level to the simulation, the resulting electrical properties are in close agreement with the measurements of a high purity epitaxial GaAs radiation detector. Also, the transferred electron effect characteristic to GaAs detectors and observed in the transient current measurements is succesfully reproduced by the simulation.

The combined results of this thesis demonstrate the versatility and power of the TCAD simulations of semiconductor radiation detectors as a tool to bridge the gap from observation to parametrization.

Acknowledgements

The work for this thesis was conducted in the CMS Upgrade Project of the Helsinki Institute of Physics. I would like to thank the entire CMS Upgrade staff for the opportunity to work and complete this thesis in such a spearheading and fascinating research project.

I am especially grateful to Dr. Jaakko Härkönen, whose project and collaboration suggestions and visionary played a crucial part in the formation of this thesis. I would also like to express my particular gratitude to Dr. Eija Tuominen, Dr. Panja Luukka and Dr. Esa Tuovinen for their invaluable help and advice. Also, I wish to thank Prof. Paula Eerola, whose directing hand initiated the whole process that has moulded and gradually crystallized over a four year period to this final product.

I feel also great gratitude towards Dr. Ulrich Parzefall and Prof. Hele Savin for reviewing this thesis and giving constructive suggestions to improve it. The readability of this thesis was considerably enhanced by the thorough language check carried out by M.A. Phyllis Peltola, of which I am deeply grateful.

Furthermore I want to express my endless gratitude towards all the members of The Silicon Sensor Simulation Working Group of the CMS Tracker collaboration. After joining the group the constant feedback and discussions accelerated my TCAD simulations learning process from baby steps to quantum leaps.

I would also like to extend my thanks to every lecturer and assistant from whom I've had the privilege to learn problem solving skills and understanding of nature. These form the ever-evolving basis that proved to be vital for the completion of this thesis.

Finally, appreciation must also be given to the several foundations, especially Waldemar von Frenckell and Vaisala, whose financial support enabled the presentation of my research in a wide range of international conferences.

Helsinki, January 26th, 2016

Timo Peltola

Abbreviations and definitions

AC	Alternating Current
ALICE	A Large Ion Collider experiment
ATLAS	A Toroidal LHC ApparatuS
C-V	Capacitance-Voltage
CCE	Charge Collection Efficiency
CERN	European Organization for Nuclear Research
CID	Current Injected Detector
CMS	Compact Muon Solenoid
CVPE	Chloride Vapor Phase Epitaxy
Cz	Czochralski silicon
DC	Direct Current
DLTS	Deep Level Transient Spectroscopy
DOFZ	Diffusion Oxygenated Float Zone silicon
DP	Double Peak
ehp	electron-hole pair
eV	electronvolt, unit of energy: 1 eV $\approx$ 1.6×10^{-19} J
fb	femtobarn, unit of area: $10^{-15} \times 10^{-28}$ m^2 = 10^{-43} m^2
Fz	Float zone silicon
GaAs	Gallium Arsenide
GaN	Gallium Nitride
HEP	High Energy Physics
HL-LHC	High Luminosity-Large Hadron Collider
I-V	Current-Voltage
IR	Infrared
LGAD	Low Gain Avalanche Detector
LHC	Large Hadron Collider
LHCb	Large Hadron Collider beauty

MCz	Magnetic-Czochralski silicon
MIP	Minimum Ionizing Particle
$n_{eq}cm^{-2}$	unit of 1 MeV neutron equivalent radiation fluence
n-type Si	silicon lattice doped with pentavalent donor atoms (e.g. phosphorus)
p-type Si	silicon lattice doped with trivalent acceptor atoms (e.g. boron)
pin	$p^+/i/n^+$, a diode structure with intrinsic bulk material
PKA	Primary Knock-on Atom
PTI	Ioffe Physical-Technical Institute
R&D	Research and Development
RD50	RD50 Collaboration 'Development of Radiation Hard Semiconductor Devices for Very High Luminosity Colliders'
SiBT	Silicon Beam Telescope
SiC	Silicon Carbide
SiO_2	Silicon dioxide
TCAD	Technology Computer-Aided Design
TCT	Transient Current Technique
TD	Thermal Donor
TSC	Thermally Stimulated Current technique

List of Publications

I **T. Peltola**, *Charge Collection Efficiency Simulations of Irradiated Silicon Strip Detectors*, Journal of Instrumentation, JINST **9** (2014) C12010.

II **T. Peltola**, A. Bhardwaj, R. Dalal, R. Eber, T. Eichhorn, K. Lalwani, A. Messineo, M. Printz and K. Ranjan, *A Method to Simulate the Observed Surface Properties of Proton Irradiated Silicon Strip Sensors*, Journal of Instrumentation, JINST **10** (2015) C04025.

III X. Wu, **T. Peltola**, A. Gädda, T. Riekkinen, J. Härkönen, P. Luukka, A. Junkes, T. Arsenovich, A. Karadzhinova, A. Winkler, P. Kostamo, S. Nenonen, E. Tuominen, H. Lipsanen, M. Mattila, *Processing and characterization of epitaxial grown GaAs radiation detectors*, Nuclear Instruments and Methods in Physics Research Section A **796** (2015), 51–55.

IV **T. Peltola**, *Silicon Sensors for Trackers at High-Luminosity Environment*, Nuclear Instruments and Methods in Physics Research Section A **796** (2015), 74–79.

V **T. Peltola**, X. Wu, J. Kalliopuska, C. Granja, J. Jakubek, M. Jakubek, J. Härkönen, A. Gädda, *Characterization of thin p-on-p radiation detectors with active edges*, Nuclear Instruments and Methods in Physics Research Section A **813** (2016), 139–146.

Author's Contributions

I Corresponding author in collaboration with the Silicon Sensor Simulation Working Group[1] and on behalf of the CMS Tracker collaboration. All presented results except for the plot in Figure 3 has been obtained by the author.

II Corresponding author presenting results acquired in collaboration with the Silicon Sensor Simulation Working Group and on behalf of the CMS Tracker collaboration. All presented work has been performed by the author.

III Corresponding author in charge of the simulation part of the study.

IV Paper written by the author on behalf of the RD50 collaboration. The simulation section highlights selected results achieved by the author within the framework of the Silicon Sensor Simulation Working Group.

V Corresponding author responsible for the simulations section of the research. Co-written with the second author.

[1]The Silicon Sensor Simulation Working Group is dedicated to simulations leading to a good sensor design for the Phase II upgrade of the CMS Tracker. The group currently includes 15 active members from 7 institutes and universities.

Contents

Chapter 1

Introduction

1.1 Background and research environment

1.1.1 Upgrade from LHC to HL-LHC

Tracking systems of High Energy Physics (HEP) experiments largely employ position sensitive silicon sensors due to their outstanding performance and cost effectiveness. They are currently installed in the vertex and tracking detectors of the ALICE, ATLAS, CMS and LHCb experiments at LHC, the world's largest particle physics accelerator at CERN[1]. The discovery of the Higgs boson in 2012 in the ATLAS and CMS experiments at CERN, was based on the success of the LHC accelerator facility and the ability of the particle detectors to record the data from the Higgs decay products.

The Compact Muon Solenoid experiment[2] (CMS) Tracker detects secondary particles from the primary proton-proton collisions with a center-of-mass energy of up to 14 TeV. The Tracker, based on Si pixel and microstrip sensors, is the largest silicon detector ever constructed and is the innermost detector of the CMS experiment, located at radii from 4 cm to 130 cm around the LHC beam pipe. The Tracker reconstructs particle trajectories that are vital in the identification process of charged particles [1]. During its nominal lifetime, the position sensitive tracking sensors, with an active area of over 200 m^2, experience a build-up of radiation damage induced by the great number of crossing particles in the detector. This leads to the degradation of the sensor properties, namely increased leakage current (I_{leak}) and full depletion voltage (V_{fd}), as well as reduced signals and resolution.

In the search for unobserved theorized phenomena, such as supersymmetric parti-

[1] http://home.web.cern.ch/
[2] http://cms.web.cern.ch/

cles, gravitons, dark matter, extra dimensions and 'micro quantum black holes' [1], the proposed upgrade of the LHC to its high luminosity phase (HL-LHC) with approximately 10-fold increase of the luminosity, will realise the maximal physics potential of the facility. However, after 10 years of operation, the integrated luminosity of 3000 fb^{-1} [2, 3, 4] will expose the all-silicon tracking systems at HL-LHC to a radiation environment that is beyond the capability of the present system design. At ATLAS and CMS, fluences of more than 1×10^{16} $\text{n}_{\text{eq}}\text{cm}^{-2}$ (1 MeV neutron equivalent) are expected for the pixel detectors at the innermost layers and above 10^{15} $\text{n}_{\text{eq}}\text{cm}^{-2}$ for the strip sensors at a radius of approximately 20 cm from vertex [1]. Since significant radiation-induced effects in the Si detector performance start to occur at fluences above 10^{13} $\text{n}_{\text{eq}}\text{cm}^{-2}$, this will require detectors with dramatically improved radiation hardness. Also, due to increased pileup (number of overlapping collision events), higher granularity sensors will be demanded. The increased granularity will call for more cost effective technologies than presently existing due to the limited resources available for the detector upgrade.

Hence, a dedicated R&D program is needed to improve current detector technologies, or develop novel ones, for both the innermost tracking layers and most of the outer tracker components with detectors that can endure higher radiation levels and higher occupancies. In addition to the experiment-specific upgrade campaigns like the CMS Phase II Tracker Upgrade, the RD50 Collaboration "Development of Radiation Hard Semiconductor Devices for Very High Luminosity Colliders"[3] (paper **IV**) was formed in 2002 with the objective to develop semiconductor sensors that meet the HL-LHC requirements. Members from several experiments at the LHC are pursuing this aim in specific research fields, namely defect/material characterization, detector characterization, new structures and full detector systems.

1.1.2 Numerical simulations

Along with measurements, simulations are an integral part of the detector development process. Their role is especially pronounced in areas like device structure optimization or prediction of the electric fields and trapping in the silicon sensors. When the numerical simulations are capable of verifying experimental results they will also gain predictive power, resulting in reduced time and cost in detector design and testing.

The main focus of the device simulations in the CMS Tracker Upgrade Project and RD50 Collaboration is to develop an approach to model and predict the performance

[3] http://cern.ch/rd50/

of the irradiated silicon detectors (diode, strip, pixel, columnar 3D) using professional software, namely finite-element Technology Computer-Aided Design (TCAD) software frameworks Synopsys Sentaurus[4] and Silvaco Atlas[5]. Among the multitude of simulation options, the TCAD packages allow the incorporation of realistic, segmented sensors in 2D or 3D, readout circuit, transient simulations with lasers or Minimum Ionizing Particles (MIP).

The simulation of radiation damage in the silicon bulk is based on the effective midgap levels, a deep acceptor and a deep donor level. The model was first proposed in 2001 and entitled later as the "PTI model" [5, 6]. The first successfully developed quantitative TCAD models, namely the proton model and the neutron model [7], for the simulation of the bulk damage characteristics like I_{leak}, V_{fd} and the Charge Collection Efficiency (CCE), were built on the basis of the PTI model.

1.1.3 Thin p-on-p pixel sensor

An advantage offered by thin silicon radiation detectors in spectroscopic applications is the good radiation differentiation which is particularly important for nuclear industry where short range particles need to be detected with high gamma ray background [8]. Also, radiation hardness is important in many nuclear safeguard applications. Further benefits of thin detectors include reduced mass, fast charge collection and some possible advantages in charge collection and reverse current after high irradiation fluences [9] due to lower drift time for a given voltage.

The planar p-type (n-on-p) silicon radiation detectors have been under extensive studies in the HEP community due to their radiation tolerance and cost effectiveness, and have become the baseline candidate to replace the conventional n-type (p-on-n) detectors for the LHC upgrade at CERN [10, 11]. The advantages of this configuration include a favourable combination of weighting and electric fields after irradiation while the readout at the n-type electrodes enables the collection of electrons which have three times higher mobility and longer trapping times than holes. The downside of the n-on-p design is the need for isolation structures between the electrodes that increase the process complexity and might lead to localized high electric fields which increase the probability of early breakdowns.

The thin p-on-p pixel detector addresses this problem without compromising CCE and spatial resolution excessively. Due to the collection of holes at the pixels,

[4] http://www.synopsys.com
[5] http://www.silvaco.com

no isolation structures are needed while the effects of low hole mobility to CCE are minimized by the reduced drift distance. Also, the expected good CCE after irradiation and an improved spatial resolution distinguish the thin p-on-p pixel detector from its thicker counterparts.

This concept could be usable also for the HEP tracking applications. To maintain low material budget and achieve high position resolution, the implementation of thin pixel detectors to the inner detector layers of the LHC experiments is foreseen for the future upgrades [12]. The thin p-on-p configuration has not been studied before in the HEP community.

1.1.4 Epitaxial GaAs radiation detector

Radiation detectors made of epitaxial GaAs are a promising alternative for the silicon devices used for spectroscopy and radiography applications requiring moderate photon energies, i.e. more than 10 keV. Mammography is an important example of such an application with large technological and societal impact. Earlier studies on using GaAs material for X-ray registration are reported e.g. in References [13, 14]. The atomic numbers of GaAs are 31 (Ga) and 33 (As) while the atomic number for Si is 14. This results in an order of magnitude higher mass attenuation coefficient for GaAs for a low energy X-ray process with a photon energy of 20 keV, leading to the photon absorption probability of 90% in a 100 μm thick GaAs while the probability is only 27% for a 300 μm thick Si.

As the basic starting material in optoelectronics industry, the processing technology of GaAs devices is well established. The epitaxy based on ultra-pure gaseous precursors is a prominent approach to fabricate pin-diode structured GaAs radiation detectors. The chloride vapor phase epitaxy (CVPE) technique has been proved to grow high purity epi-GaAs with a high growth rate (about 10 μm/hour) and with an achievable layer thickness of more than 100 μm, as is required in detector applications.

Radiation detectors were processed on GaAs substrates with 110 μm - 130 μm thick CVPE grown epitaxial absorption volume. In the characterization process, the Deep Level Transient Spectroscopy (DLTS) analysis revealed a significant concentration of deep level electron traps in the epitaxial layer. Also, the transferred electron effect [15, 16, 17], where the drift velocity of charge carriers decreases after the electric field inside the GaAs material has reached the value of about 3.3 kV/cm [15], was observed in the transient response. Numerical simulations were conducted to verify the results and to further analyse the observed behaviour. No previous comparative

simulation studies on the transient response of the GaAs detectors have been published.

1.2 Objectives and scope

The primary theme of this thesis is to establish the versatility and importance of the numerical TCAD simulations in semiconductor research. For the work, a commercial Synopsys Sentaurus finite-element Technology Computer-Aided Design (TCAD) software framework was applied.

The first aim is to develop a simulation model for the radiation damage in silicon strip sensors using the data obtained from sensors after irradiation. The goal of the radiation damage model is to provide a comprehensive set of both bulk and surface properties that reflect the measurements and predict the strip sensor performance in the expected fluence range of the HL-LHC. Also, an essential objective of the model is to provide an interpretation of the processes leading to the observed surface characteristics in the irradiated position sensitive planar sensors. Understanding the macroscopic effects of the microscopic defects is of particular importance in the radiation hardness studies for the future CMS Tracker.

The second objective of this thesis is to provide novel qualitative information of a thin p-on-p pixel sensor and compare the results with a more conventional p-on-n pixel sensor of similar design. Complementing a comparative simulation study of the electric field evolution with voltage and breakdown behavior, an interpretation of the measured difference in the charge collection is pursued as well. Since no previous studies on the configuration exist in the HEP community and at the prospect of the thin pixel sensor implementations to the inner detector layers of the LHC experiments for the future upgrades, the results could be considered as an introduction of the thin p-on-p pixel sensor as an option for the HEP tracking applications.

The third goal is to expand the TCAD simulations from the elemental material of Si to a compound semiconductor material in order to verify and further investigate the measurements of newly processed GaAs radiation detectors. Under specific scrutiny are the reproducibility of the electrical measurements via the insertion of a deep defect level to the simulation as well as the influence of the transferred electron effect to the transient signals. Due to shortage of published simulation studies on the subject, this investigation could serve as an argument for the increased role of the device simulations in the GaAs radiation detector research.

The scope of this thesis includes research of both HEP and spectroscopy applications of the semiconductor radiation detectors. Simulated structures are limited to strip and

pixel sensors as well as diodes. Due to the lack of available measured data of the CCE loss between the strips with respect to different geometries and fluences, the presented parametrization of the 'non-uniform 3-level model' is restricted to the specific strip pitch of 120 μm and the fluence range of $(0.3 - 1.4) \times 10^{15}$ $\mathrm{n_{eq}cm^{-2}}$.

The highest fluences, about 2×10^{16} $\mathrm{n_{eq}cm^{-2}}$, expected for the pixel and 3D columnar detectors closest to the vertex at the HL-LHC, are not considered in the study since no validated radiation damage model above the upper limit of the aforementioned fluence range exists.

1.3 Research process and dissertation structure

The thesis starts with an introduction to the background and objectives of the research in chapter 1. The basics of silicon used as a particle detector are explained in chapter 2 including its HEP and spectroscopy applications. The radiation damage and its impact on silicon detectors is described in chapter 3. The simulation of radiation damage in segmented sensors is introduced and discussed at the end of the chapter. This includes the description of the applied Sentaurus TCAD simulation package and the implementation of a basic device simulation.

The results from the several studies included in the thesis are presented and discussed in chapter 4. First, the development of the effective non-uniform 3-level defect model, a radiation defect model that combines experimentally matching surface damage properties with the validated bulk damage properties of the proton model [7], is presented. By comparing the simulated results like the interstrip resistance (R_{int}) and capacitance (C_{int}) as well as the position dependence of CCE (CCE(x)) of strip sensors with the real data at every step of the development process, the chosen parameter values are justified. The research is also viewed in the context of the recent efforts in the scientific program of the RD50 Collaboration. A brief insight into the development path from the observed defects to the effective defect model and from the initial 1-dimensional model for custom-made software to the quantitative TCAD models is provided.

Next, a comparative measurement and TCAD simulation study of a thin p-on-p pixel sensor with a more conventional p-on-n pixel sensor of similar design is presented. Electrical characteristics are investigated in detail by looking at the simulated C-V, I-V, interpixel resistance and electric field distribution results of the two sensor types. Carrier lifetime tuning is decribed as a method to reproduce and interpret the measured differences in the charge collection.

The final section in chapter 4 covers the results of the characterization and device simulations of the 110 μm thick epitaxial pin-diode GaAs radiation detector. The reproduction of the observed C-V and I-V results via the insertion and tuning of a deep defect level to the simulation is explained. A simulation study of the influence of the transferred electron effect to the transient signals produced by a red laser injection is also presented.

The discussion in chapter 5 consists of the possible theoretical and practical implications of the work and the assessment of the reliability and validity of the results and applied methods. Finally, recommendations for further research are given.

Chapter 2

Silicon radiation detector

Several characteristics of semiconductor radiation detectors, including compact size, high energy resolution, fast timing characteristics and variable effective thickness, are superior to other radiation detector types. Of the semiconductor materials especially silicon (Si) has been widely used in HEP research such as the LHC experiments at CERN, due to its cost efficiency and excellent position accuracy.

Basic features of the silicon sensors allow operation in temperatures ranging from cryogenic to room temperature. However, variations in temperature change the resistivity of the semiconductor, affecting the leakage current and hence the noise in the sensors. Therefore, cooling is typically used to minimize leakage current as well as to avoid high noise and thermal runaway in the case of irradiated sensors.

The size of a silicon sensor can be a limiting factor in applications where large surface area is required. The capacitance of a Si diode grows with the size of its surface area, resulting in decreased energy resolution. Hence, the usual surface sizes range from 1 to 5 cm^2. However, for the highly segmented detectors described in this thesis, area is of no concern. Depletion depths (bulk volumes emptied from free charge carriers) of 5 mm can be reached commercially, but are commonly limited to a few hundred micrometers [18].

When designed as position sensitive detectors, Si sensors at the LHC are vital in the identification of charged particles by providing information about the position and momentum of the particles. The fast collection of the signals generated by the ionizing particles (about 10 ns, depending on the sensor thickness) in thin silicon sensors, enables the operation of the detectors at the LHC's high bunch crossing rate of 40 MHz.

Despite the substantial inherent radiation tolerance of the silicon sensors, significant changes to the performance start to occur at fluences above 10^{13} $n_{eq}cm^{-2}$. Therefore,

current detectors do not last the planned 10 years in the HL-LHC radiation environment. However, different silicon bulk materials, detector designs and engineering techniques may extend the application of Si detectors to the domain of the HL-LHC fluence level.

This chapter gives a description of the basic working principles of a silicon sensor and its use in different detector configurations and applications. The discussion is extended to radiation hardness and the simulation of radiation-induced defects in the following chapter.

2.1 Operation of silicon radiation detector

A silicon particle detector is constructed by forming a reverse biased pn-junction. With increasing bias voltage, the electric field region sensitive to particles extends from the junction further into the detector volume. Electron-hole pairs generated by the ionizing particle in the field region are collected at the anode and cathode electrodes. To acquire position data, the charge collecting electrodes are segmented.

In the following, a short summary of the features of the pn-junction and the most essential properties with respect to the charge collection are given.

2.1.1 pn-junction

The real pn-junction is typically approximated as an abrupt junction [19], where the net dopant density changes from one to another as in a step function. Net charge formed inside the region of the pn-junction establishes a potential difference across the junction. The value of the potential φ is found by solving the Poisson's equation in one dimension [18]

$$-\frac{d^2\varphi}{dx^2} = \frac{dE}{dx} = \frac{\rho(x)}{\epsilon_s}, \tag{2.1}$$

where E is the electric field, $\rho(x)$ is the net charge density and ϵ_s is the permittivity of the semiconductor material. For space-charge distribution of figure 2.1

$$\rho(x) = \begin{cases} eN_{\mathrm{D}}, & -a < x \leq 0 \\ -eN_{\mathrm{A}}, & 0 < x \leq b \end{cases}, \tag{2.2}$$

where e is elementary charge and N_{D} and N_{A} are donor and acceptor atom densities, respectively. By combining the equations 2.1 and 2.2, and requiring that the electric field $E(x)$ must vanish at both edges of the charge distribution, $E(x)$ shown in

figure 2.2a is now given by

$$E(x) = \frac{d\varphi}{dx} = \begin{cases} -\frac{eN_\mathrm{D}}{\epsilon_s}(x+a), & -a < x \leq 0 \\ \frac{eN_\mathrm{A}}{\epsilon_s}(x-b), & 0 < x \leq b \end{cases}. \tag{2.3}$$

The electric field is now linearly dependent of x and has a maximum E_max at the pn-interface $x = 0$, where equations 2.3 must match

$$E_\mathrm{max} = |E(x=0)| = \frac{eN_\mathrm{D}a}{\epsilon_s} = \frac{eN_\mathrm{A}b}{\epsilon_s}. \tag{2.4}$$

The width of the space charge region W is then

$$W = a + b = E_\mathrm{max}\frac{\epsilon_s}{e}(\frac{1}{N_\mathrm{D}} + \frac{1}{N_\mathrm{A}}). \tag{2.5}$$

With boundary conditions φ(-a) = V and $\varphi(b) = 0$ the potential across the junction, as shown in figure 2.3, is given by

$$\varphi(x) = \begin{cases} -\frac{eN_\mathrm{D}}{2\epsilon_s}(x+a)^2 + V, & -a < x \leq 0 \\ \frac{eN_\mathrm{A}}{2\epsilon_s}(x-b)^2, & 0 < x \leq b \end{cases}, \tag{2.6}$$

where $V = V_\mathrm{c}$–V_ext, the difference between contact potential of the junction and applied external bias voltage. Requiring match at $x = 0$ for equations 2.6 and using equation 2.4, the voltage drop in the diode can be expressed as

$$V = V(x=0) = \frac{eN_\mathrm{D}a^2}{2\epsilon_s} + \frac{eN_\mathrm{A}b^2}{2\epsilon_s} = \frac{1}{2}E_\mathrm{max}(a+b) = \frac{1}{2}E_\mathrm{max}W. \tag{2.7}$$

Combining the equations 2.5 and 2.7 and looking at the typical case of one-sided junction, where e.g. $N_\mathrm{A} \gg N_\mathrm{D}$, the width of the whole depletion region is given as

$$W \cong \sqrt{\frac{2\epsilon_s V}{eN_\mathrm{B}}}, \tag{2.8}$$

where N_B is the doping density of the material with lighter dopant concentration.

Since the equation 2.4 indicates that the net charge is zero, it follows that $a \gg b$ and therefore $W \cong a$. In the typical detector structure, this region forms the bulk that acts as a detection volume. One-sided junction, i.e. a *rectifying contact*, illustrated in figure 2.2b, enables the full depletion of the bulk material with lowest possible reverse bias voltage. Adding heavily doped implant of the same type as the detection material to the opposite side of the bulk, e.g. $\mathrm{p}^+/\mathrm{n}^-/\mathrm{n}^+$, forms a *blocking contact* that minimizes the leakage current across the junction.

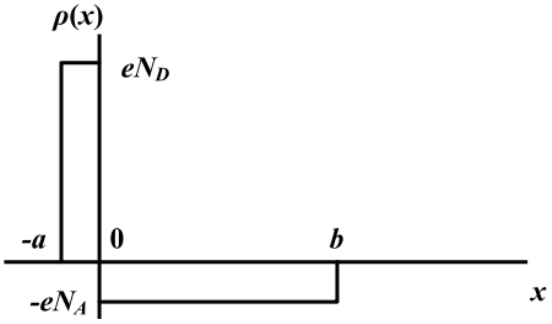

Figure 2.1: An idealized space-charge distribution for the case where $N_{\mathrm{D}}>N_{\mathrm{A}}$. Electron diffusion results in a positive space charge in the region -a $< x \leq$ 0 and the filled acceptor sites correspond to the negative space charge at $0 < x \leq$ b.

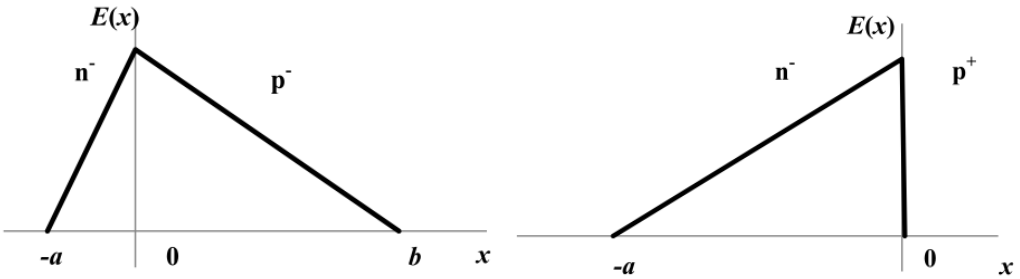

(a) (b)

Figure 2.2: (a) The shape of the electric field corresponding to the space-charge distribution of figure 2.1. Because of the higher doping concentration level of n-type material, the electrons tend to travel greater distance into the p-type material before recombination. This extends the electric field farther into the p-side. (b) The electric field distribution of the pn-junction when $N_{\mathrm{A}} \gg N_{\mathrm{D}}$, i.e. p^+/n. The depletion region is essentially on the n-side of the pn-junction, but for typical dopant concentrations still extends a few nm to the heavily doped side.

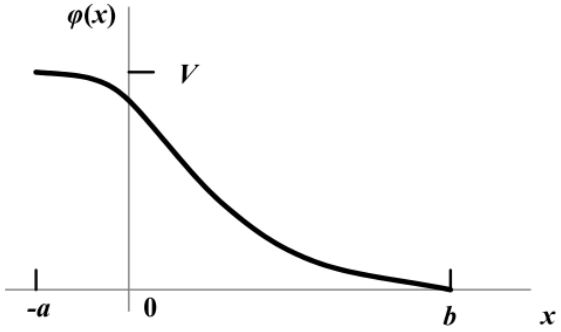

Figure 2.3: The potential distribution across the pn-junction achieved by integrating $E(x)$ with boundary conditions $\varphi(-a) = V$ and $\varphi(b) = 0$.

2.1.2 C-V and I-V Characteristics

The theory presented in this section is based on reference [17]. The depletion capacitance per unit area of a pn-junction is defined as the change in the charge of the depletion layer per unit area dQ to the variation in the applied voltage dV. Since charge increases the electric field by $dE = dQ/\epsilon_s$ and the corresponding variation of the applied voltage is approximately $dV = WdE$, capacitance per unit area becomes

$$C = \frac{dQ}{dV} = \frac{\epsilon_s}{W} = \sqrt{\frac{e\epsilon_s N_{\mathrm{B}}}{2V}}, \tag{2.9}$$

where the last term is achieved using equation 2.8 for W.

In a fully depleted pn-junction Si diode the depletion depth W equals the wafer thickness d. Once the wafer is fully depleted, the capacitance reaches its minimum. This is due to the effect of the increased reverse bias voltage on the fixed charges that are built up on each side of the junction, i.e. with growing depletion region the capacitance represented by the separated charges decreases [18]. Capacitance per unit area C_{fd} is then equal to the geometrical capacitance C_{geo},

$$C_{\mathrm{fd}} = C_{\mathrm{geo}} = \frac{\epsilon_s}{d}, \tag{2.10}$$

due to being solely dependent on the size of the diode junction.

By plotting capacitance-voltage data as a (V, C^{-2}) graph, shown in figure 2.4, it is possible to determine the voltage required to extend the electric field through the entire wafer thickness, i.e. the full depletion voltage V_{fd}. Extracted from the C-V measurements, V_{fd} data allows the determination of the approximate value of the effective doping concentration in the silicon bulk. By combining the equations 2.9

and 2.10 it is given by

$$N_{\mathrm{B}} = \frac{2\epsilon_s}{ed^2} V_{\mathrm{fd}}, \tag{2.11}$$

where W and V has been replaced by d and V_{fd}, respectively.

When biasing the pn-junction with reverse voltage, in an ideal case, the resulting reverse leakage current is dominated by the diffusion current J_{diff} approximated by the Shockley equation [20]. In a real diode of detector-grade silicon material, the generation current in the depletion region J_{g} is the dominating component at any voltage and the reverse leakage current density J_{R} is essentially

$$J_{\mathrm{R}} \simeq J_{\mathrm{g}} = \int_0^W e|U|dx \simeq e|U|W = \frac{en_{\mathrm{i}}W}{\tau_e}, \tag{2.12}$$

where U is the rate of electron-hole pair generation, n_{i} is the intrinsic charge carrier concentration and τ_{e} is the effective electron lifetime. Factor n_{i} suggests that only energy levels near the intrinsic Fermi level contribute significantly to the generation rate U. Both τ_{e} and n_{i} have considerable dependence on temperature T, but if τ_{e} is a slowly varying function of T, J_{g} will then have the same dependence on temperature as n_{i}.

By replacing W in equation 2.12 with the equation 2.8 it is thus expected that

$$J_{\mathrm{g}} \sim (V_{\mathrm{c}} - V_{\mathrm{ext}})^{1/2} = \sqrt{V}, \tag{2.13}$$

at a given temperature for an abrupt pn-junction.

2.1.3 Particle detection

While travelling through the detector, energy deposited by the particle generates within a few picoseconds equal numbers of conduction electrons and holes along the particle track, presented in figure 2.5. Electric field present throughout the active volume ensures that both charge carriers feel the electrostatic forces causing them to drift in opposite directions. The motion of the charge carriers constitutes a current that will persist until they are collected at the electrodes on both sides of the depletion region [18].

The average energy required to create an electron-hole pair (*ehp*) in silicon is 3.62 eV in room temperature, even though the bandgap is 1.12 eV. Since silicon is an indirect semiconductor, i.e. the transition from the valence band to the conduction band requires a change in crystal momentum for the electron $\vec{p}_{\mathrm{cr}} \equiv \hbar\vec{k}$, where $\hbar$ is the

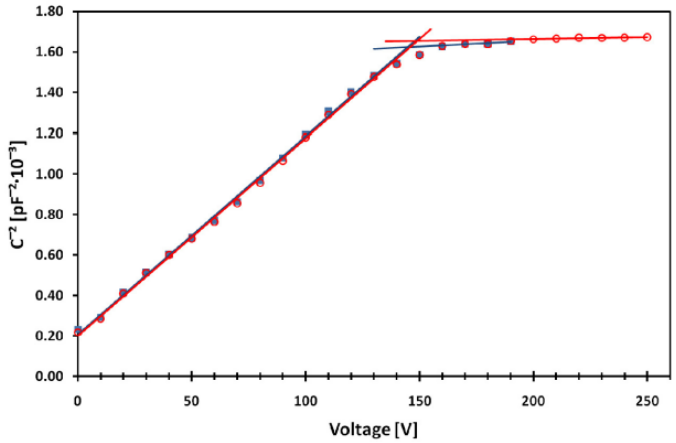

Figure 2.4: The principle of the full depletion voltage V_{fd} determination from (V, C^{-2}) graph. V_{fd} is extracted from the crossing point of the linear fits made to the dynamic and plateau regions of the curve. Measurement error is determined from the standard deviation of repeated measurements.

reduced Planck's constant and $\vec{k}$ is the wave vector of the lattice, the energy difference goes to phonons and plasmons needed to compensate the momentum changes [17].

To reach full depletion of the lightly doped n-type bulk material of figure 2.5 with lowest voltage possible, a junction with heavily doped p-type layer is formed on the front surface of the detector. Benefits for the electric field distribution of this rectifying contact were discussed in section 2.1.1, but because of its low minority charge carrier concentration, it also serves as a blocking contact that prevents the electrons removed by the electric field on the back surface electrode from being replaced at the opposite electrode.

Because the minority charge carriers are not highly suppressed in the bulk of the detector, an additional blocking contact is also needed on the back surface electrode. Implantation heavily doped with donor impurities minimizes the hole injection through the bulk when they are collected on the front surface electrode. This way the non-injecting conditions to suppress bulk leakage current are provided on both surfaces.

The signal level of a fully depleted, non-irradiated detector depends then exclusively on the wafer thickness d as [18]

$$n_{\mathrm{ehp}} = \frac{dE}{dx}\frac{d}{E_{\mathrm{a}}}, \tag{2.14}$$

where n_{ehp} is the number of generated electron-hole pairs, dE/dx is the mean rate of particle energy loss in silicon as given by the Bethe-Bloch equation [18] and E_{a} is the

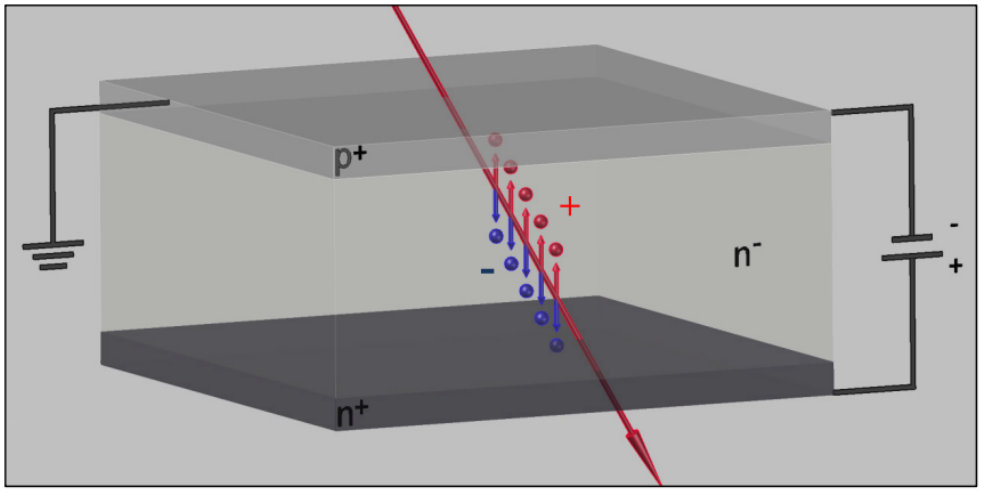

Figure 2.5: Operation principle of the silicon particle detector. Charged particle generates electron (blue)-hole (red) pairs that move through the electric field of the depletion region. Holes and electrons are collected at the cathode and anode, respectively. p^+/n^+ indicates a layer heavily doped with acceptor/donor impurities while n^- is lightly doped n-type bulk material.

activation energy required for *ehp* creation.

The guard ring structure surrounding the active area of the detector prevents the lateral expansion of the electric field with increased depletion voltages, thus providing precisely defined active volume. Without the guard ring structure, the electric field could reach the detector edges damaged by the dicing process, attracting high external currents into the sensitive region [18, 19] and degrading the signal-to-noise ratio of the sensor.

2.2 Tracking sensors

In applications involving charged particles, silicon is typically selected as the detector material. When the incident particles have sufficient energy to pass completely through the wafer, the Si detectors can be used as transmission detectors. Then the pulse amplitude indicates the energy lost by the incident radiation during its transit through the device [18]. This is the case for the tracking detectors in HEP applications, where the particles of interest have energies of at least several hundred MeV that will enable them to pass with ease through all the tracking layers of e.g. the CMS Tracker. Positional data in the particle tracking systems is acquired via segmenting the surface electrodes of the sensor as in strip and pixel detectors or by processing electrode

columns into the sensor bulk as in 3D columnar detectors.

2.2.1 Planar sensors

By segmenting the front surface implantation, the silicon strip and pixel detectors are applied in particle tracking systems of HEP experiments. This configuration produces the maximum of the electric field to the segmented side, which is desirable to acquire fast and accurate positional data of the charged particle passing through the sensor. The 1–10 cm long strip sensors at the CMS Tracker provide very accurate measurement of the position perpendicular to the strips since the strip pitch is typically between 70–240 μm, while the current pixel sensor size is 100 μm by 150 μm.

Thus, a single-sided strip sensor measures one coordinate of the traversing particle and the strip sensors have to be arranged in an angle with each other at different radii in the CMS Tracker to provide 2D information while the corresponding position data is obtained from a single pixel sensor. The small size of the pixel electrodes results also in a relatively small capacitance and leakage current leading to considerably reduced electronic noise compared to a microstrip detector of equivalent dimensions [18].

Once collected at the opposite contacts, electrons within about 10 ns and holes about 25 ns in a typical detector of 300 μm thickness [18], the charge is measured with the readout electronics. Strip detectors used in LHC experiments are AC-coupled. The drawback of leakage current access to read-out electronics in the traditional DC-coupled detectors is avoided in AC-coupling by separating and reading the signal current through a simple high-pass filter. The signal is read through a strip capacitor and the leakage current is conducted through a bias resistor to the common bias line, which is grounded [19].

The DC-coupled pixel detector chips are connected to a separate readout chip by flip chip solder bonding that amplifies the signal.

2.2.2 3D columnar sensors

The 3D columnar sensors are likely to be the most promising choice for the extremely high fluence environments. By having doped columns etched into the silicon bulk vertically to the device surface, the geometry of the 3D sensors decouples the depletion voltage and the detector thickness. This means that also the charge drift length is decoupled from the ionization path, i.e. the drift length is now the inter-column spacing, while the signal is still proportional to the detector thickness resulting in a higher radiation tolerance [21].

The downsides of the 3D sensors are the complexity of the processing, the higher inter-electrode capacitance (with higher electronics noise), non-sensitive regions in the columns and the hit position dependent signal size. The disadvantage of the low-field regions can be resolved by the 3D trench electrode detectors that have a concentric trench electrode surrounding the central hexagonal signal collecting column electrode [22, 23]. This design results in an uniform electric field. In addition to the single column type [24], a double column-double sided technology has been developed by the RD50 institutes [25].

2.3 Spectroscopy semiconductor sensors

Advantages offered by semiconductor detectors for the spectroscopy applications include exceptionally good energy resolution, good stability and absence of drift, excellent timing properties, very thin entrance windows along with simplicity of operation [18]. Radiation hardness in these applications is not an issue because of low fluence levels and they typically include the spectroscopy of alpha particles and fission fragments as well as gamma and X-ray radiation. The desired sensor parameters are now large active volume together with high charge carrier mobilities, high atomic number and operation without cooling apparatus [18]. With appropriate depletion voltage that optimizes the carrier mobilities, the CVPE grown epitaxial GaAs detector studied further in section 4.3 fits all these conditions.

Since the position information is now irrelevant, the sensor structures in spectroscopy are typically simple pad diodes.

2.4 Applications

Applications of radiation hard silicon detectors are not restricted to HEP experiments. Improved radiation hardness leads to longer reliable detection lifetime that is a desirable feature in the semiconductor detectors used in satellites and space probes where maintenance cannot be performed.

In medical procedures such as diagnostic radiography, X-ray tomography and radiation therapy, parts of human body are exposed to high fluxes of ionizing radiation. For example, in an application using a synchrotron light source [26], the X-ray pictures produced by silicon strip detectors show excellent contrast and the required dose is lower when compared to conventional film use [27]. Si detectors of high radiation hardness would provide an easy and accurate way to determine doses received by the

patient without the disadvantage of time and resource consuming recalibrations caused by detector performance degradation. The drawback of Si in such applications with moderate photon energies is the low absorption efficiency linked to the low atomic number (Z) when compared to high-Z materials like CdTe or GaAs.

Chapter 3

Radiation hardness

3.1 Radiation-induced damage

Radiation levels above $\sim 10^{13}$ $n_{eq}cm^{-2}$ cause damage to the silicon crystal structure. Fluences above 1×10^{14} $n_{eq}cm^{-2}$ lead to significant degradation of the detector performance. In the intense radiation fields of the LHC, defects are introduced both in the silicon substrate (bulk damage) and in the SiO_2 passivation layer that affect the sensor performance through the interface with the silicon bulk (surface damage). Bulk damage degrades detector operation by introducing deep acceptor and donor type trap levels [28]. The main macroscopic effects of bulk damage on high-resistivity silicon detectors irradiated by hadrons are the change of the effective doping concentration N_{eff}, the increase in the leakage current proportional to the fluence and the degradation of Charge Collection Efficiency (CCE) [29].

Due to the radiation-induced generation of deep acceptor levels in the band-gap, negative space charge is produced and $|N_{\text{eff}}|$ of the n-type silicon substrate is reduced leading to the eventual change of the space charge from positive to negative. The pn-junction and thus, the electric field maximum shifts then to the n-contact on the back surface of the type inverted detector. However, the electric field distribution is vastly non-uniform at the irradiation fluences beyond 10^{14} $n_{eq}cm^{-2}$ and has a double peak shape for all Si detector types. The overall negative space charge after HL-LHC fluences requires well over 1 kV for a full depletion of a 300 μm thick detector [30].

The high concentration of trapping centers leads to reduced effective carrier drift length which at an electric field strength of 1 $V\mu m^{-1}$ is about 140–190 μm for electrons and 50–80 μm for holes after fluence of 10^{15} $n_{eq}cm^{-2}$ [29,31]. Trapping and incomplete depletion result in significant deterioration of CCE and increase in the leakage current,

which leads to degrading signal-to-noise ratio [32].

The increase of the bulk generation current ΔI, caused by the damage created generation-recombination centers, is dependent on the irradiating particle type and fluence. When normalized to the sensitive volume V the reverse current measured at full depletion is proportional to the 1 MeV neutron equivalent fluence Φ_{eq}[1]. *Current-related damage rate* α is then defined by [33, 30]

$$\frac{\Delta I}{V} = \alpha \cdot \Phi_{\mathrm{eq}}. \tag{3.1}$$

The measured value of the ΔI depends exponentially on the operating temperature and values of α are therefore always normalized to 20° C [34]. The temperature normalized damage rate α is a universal constant at any given temperature and annealing time, independent of the material type or irradiating particles (neutrons, protons, pions). Thus, α is used to reliably monitor the accumulated particle fluence.

The bulk damage in silicon detectors is primarily due to displacing a Primary Knock-on Atom (PKA) out of its lattice site resulting in a pair of a silicon interstitial and a vacancy (Frenkel pair), with a threshold energy of ∼25 eV. These can migrate through the lattice and form point defects with impurity atoms. Both point defects and clusters are responsible for the various damage effects in the detector bulk, depending on their concentration, energy level and the respective electron and hole capture cross section. Low-energy recoils above specific particle threshold energies will usually create fixed point defects. At recoil energies above ∼5 keV, a dense agglomeration of defects is formed at the end of the primary PKA track. These disordered regions are referred to as defect clusters [34, 33].

Measurements with methods like Thermally Stimulated Current technique (TSC), Deep Level Transient Spectroscopy (DLTS), Transient Current Technique (TCT) along with the C-V and I-V measurements have revealed a multitude of defects (11 different energy levels listed in [35]) after irradiations with hadrons or higher energy leptons. The microscopic defects have been observed to influence the macroscopic properties of a silicon sensor by charged defects contributing to the effective doping concentration [36, 37, 38, 39, 40, 41] and deeper levels also to trapping and generation/recombination of the charge carriers (leakage current) [41, 42, 43, 44].

[1]Non-ionizing energy loss (NIEL) scaling hypothesis offers the opportunity to normalize the different radiation effects of various particles over large energy range to the displacement damage cross-section of 1 MeV neutrons. Though not a strict rule, NIEL scaling nevertheless provides a useful tool to compare most particles and energy dependence of the damage observed in silicon particle detectors [30].

Surface damage consists of a positively charged layer accumulated inside the oxide and of interface traps created close to the interface with silicon bulk [45,46]. High oxide charge densities Q_{f} are detrimental to the detector performance since the electron layer generated under the SiO_2/Si interface can cause very high electric fields $E(x)$ near the p^+ strips in p-on-n sensors and loss of position resolution in n-on-p sensors by providing a conduction channel between the strips. High $E(x)$ can induce detector breakdown or avalanches that can result in non-Gaussian noise events. Also the increase of interstrip capacitance C_{int} with the accumulating interface charges will contribute to higher strip noise. Additionally, the position dependence of the charge collection efficiency CCE(x) has been observed to result in up to ∼30% CCE losses between the strips in heavily irradiated sensors [47, 48]. In the study presented in this thesis (papers **I, II**) this has been related to the effects of the interface traps N_{it}.

3.2 Radiation hard detectors

Future very high luminosity colliders, such as the upgrade of the LHC to a 10-fold increased luminosity of 10^{35} $\mathrm{cm}^{-2}\mathrm{s}^{-1}$, will require semiconductor detectors with substantially improved properties. Considering the expected total fluences of fast hadrons, the detector must be ultra radiation hard, provide a fast and efficient charge collection and be as thin as possible within the limits of acceptable signal and noise levels [1, 29].

Technologies studied by CERN's RD collaborations include defect and material engineering by RD48 and RD50, device engineering by RD50, operational mode engineering by RD39 and application of materials other than Si by RD42 [29].

Research topics include the improvement of the intrinsic radiation tolerance of the sensor material and novel detector designs with benefits like reduced trapping probability (thinned and 3D sensors), maximized sensitive area (active edge sensors) and enhanced charge carrier generation (sensors with intrinsic gain).

The following sections showcasing the several R&D approaches for radiation hard detectors are mostly based on the results presented in (paper **IV**).

3.2.1 Defect and material engineering

Deliberate modification of the detector bulk material is known as material engineering. It includes defect engineering where impurities are added to silicon in order to affect the formation of electrically active defect centers and thus control the macroscopic

parameters of devices.

One of the most successful examples for defect engineered silicon is oxygen-enriched silicon [29]. Oxygenation can be achieved during the crystal growth or by high-temperature long-time oxygenation process.

In Diffusion Oxygenated Float Zone (DOFZ) silicon the diffusion of oxygen into the silicon bulk is made from an oxide layer grown via a standard oxidation step. When irradiated with highly energetic charged hadrons, the build-up of negative space charge is strongly suppressed. Oxygen atoms increase the radiation hardness of a detector by capturing vacancies, forming vacancy-oxygen complexes and thus slowing the leakage current increase and donor removal [49].

The intrinsically high interstitial oxygen concentration of the order of $10^{17} - 10^{18}$ cm^{-3} in Czochralski silicon (Cz) gives it potentially better radiation hardness properties than for the standard Float zone (Fz) and DOFZ silicon (DOFZ [O] $\approx 1 - 4 \times 10^{17}$ cm^{-3}) [19]. Cz-Si's resistance for type inversion and overall smaller increase in depletion voltage compared to oxygenated or standard Fz silicon is believed to be caused by the formation of donors (most probably thermal donors), which overcompensate the radiation induced acceptors [50]. Furthermore, it has been observed that in the n-type magnetic Cz (MCz) material neutron and proton irradiations introduce effects that act as doping of opposite polarity, resulting in a potential partial cancellation effect of the degradation of N_{eff} [9].

However, after neutron irradiation, no effect or only small influences [33] of the oxygenation on the radiation hardness have been observed. Also, the effective trapping times and leakage current are not significantly influenced by the oxygen content after hadron irradiation [51, 50]. A drawback of a material with very high oxygen content is that it requires special attention to avoid thermal donor creation and thus a change of N_{eff} during processing.

Other approaches in defect and material engineering include the use of epitaxial silicon or silicon enriched with oxygen dimers [52], hydrogen or other impurities like germanium.

Since it is possible that fluences above 10^{16} $\mathrm{n_{eq}cm}^{-2}$ correspond to the operating limit of silicon sensors at temperatures close to room temperature, other semiconductor sensor materials are under investigation. These include diamond [53], silicon carbide (SiC) [29] and the semi-insulating GaN [54] detectors, which have recently been recognized as potentially radiation hard.

3.2.2 Device engineering

Improvement of detector structures, known as device engineering, includes modification of the electrode configuration, thinning of the bulk material, using p-type material and the development of new detector geometries such as 3D columnar detectors.

Thin detectors Thinning down planar detectors to about 50 μm thickness provides reduced depletion voltage. At fluences above 10^{15} $n_{eq}cm^{-2}$ thin sensors have an advantage over thicker sensors that cannot reach full depletion at plausible voltages anymore due to the high value of N_{eff} [9]. A further advantage at very high fluences is the relation to trapping due to the drift distance. In thicker detectors, more signal charges get trapped on their longer drift path to the electrodes. Hence, the ratio of measured signal in thin and thick detectors becomes more advantageous for thin sensors once trapping dominates.

However, the collected absolute charge is strongly reduced, setting higher requirements on the readout electronics. This makes the reduction of the detector thickness a compromise between the full depletion requirement and the amount of *ehp*s generated in silicon bulk [29, 10, 55]. Since electronic noise grows with increasing capacitance and the signal level decreases linearly as a function of thickness, the prospects of reducing the detector thickness from present day applications is very limited.

N-on-p sensors Much studied approach to improve the radiation hardness of the silicon particle detectors is the application of $n^+/p^-/p^+$ (n-on-p, n-in-p) structures instead of the conventional p-on-n configuration [10, 56]. Since radiation introduces acceptor-like defects, as discussed in section 3.1, no type inversion occurs in the p-type bulk resulting in a favourable combination of the weighting and electric fields after irradiation. The readout at n-type electrodes leads to a signal dominantly generated by electrons. Since electrons have three times higher mobility and longer trapping times than holes, the amount of trapped charge carriers during their drift is reduced. This allows high speed readout and higher CCE in p-type devices than in conventional detectors [10]. When p-type Cz-Si is used as a starting material, it is possible to adjust the full depletion voltage of the detector by the introduction of thermal donors (TD). TDs are complexes consisting of four or more oxygen atoms that, by compensating some of the initial acceptors, lead to lower initial operating voltages [19]. Another asset of the p-type sensor is the reduced dependence of CCE from the reverse annealing of the effective space charge in highly irradiated detectors [11, 31].

The disadvantage of n-on-p devices is the more complex fabrication technology due to required isolation structures between the n-electrodes [56]. High doping concentrations in the isolation implantations can also lead to localized high electric fields that increase the probability of early breakdowns. On the other hand, the electric fields at the n^+-strips are lower than in n-bulk sensors.

After long-term measurement campaigns accompanied by TCAD simulation studies (shown in reference [57]) the planar n-on-p sensors have become the baseline for the ATLAS and CMS strip tracker upgrades for the outer layers with maximum fluences of approximately 2×10^{15} $n_{eq}cm^{-2}$.

3D columnar detectors In the 3D-columnar design [21, 32], discussed in section 2.2.2, the maximum drift distance of the charge carriers and depletion depth depend on the electrode spacing rather than the detector thickness. Compared to the planar technology strip and pixel detectors with electrodes confined to the detector surface, the advantages of 3D structure include shorter collection distances, faster collection times and lower depletion voltages, depending on the electrode diameter and pitch chosen. This makes the 3D columnar detectors resistant to radiation induced increase of depletion voltage and charge carrier trapping in the silicon bulk. The drawbacks of 3D columnar detectors were discussed in section 2.2.2.

Due to recent availability in mass production and an acceptable signal yield after irradiation to fluences of 1×10^{16} $n_{eq}cm^{-2}$, the 3D sensors now populate 25% of the ATLAS experiment's insertable b-layer (IBL) [58].

Sensors with intrinsic gain The effect of charge multiplication has been observed in several device types, namely the strip sensors, 3D sensors and diodes [59, 60, 61]. The enhancement arises from the carrier avalanche multiplication in the high electric field of the junction, which results from a high negative space charge concentration in the bulk after irradiation [62].

To understand the underlying mechanisms of the multiplication and to optimize the CCE performances, dedicated charge multiplication sensors have been fabricated. The sensors with intrinsic gain, i.e. Low Gain Avalanche Detectors (LGAD), are based on avalanche photodiode technology and feature an implemented multiplication layer, a deep p^+ implant below the cathodes. An edge termination done by a low doping n-well is needed to secure gain uniformity [63].

Gain values of up to $\sim$20 have been measured [64] in the non-irradiated LGADs while the leakage current and noise are independent of the gain [65]. With this

technology, thinner detectors can be produced to give the signal of thick ones, enabling the investigation of ultra-fast detectors [66, 67] for HL-LHC. This requires first a solution to the significant reduction of gain after irradiations to expected fluences. Instead of trapping, the effective acceptor removal in the p^+ layer is responsible for the gain degradation by reducing the electric field [64].

3.2.3 Variation of detector operational conditions

Study of optimal detector operational conditions include the operation of silicon detectors at cryogenic temperatures or in current injected mode.

Irradiated Si-detectors are typically cooled moderately to lower the leakage current and to reduce reverse annealing [68]. When cooling is extended to cryogenic temperatures, trapping and de-trapping of the carriers in radiation induced levels modifies the effective concentration N_{eff} of the ionized charges. This will in turn change the electric field distribution and thus affect the CCE.

At cryogenic temperatures, the de-trapping rate of electrons and holes is strongly affected by the reduced thermal energy. When the de-trapping time is considerably longer than the shaping time of the read-out electronics, trapping of the drifting charges becomes the predominant effect. This leads to reduced $|N_{\text{eff}}|$ and to the condition where a consistent fraction of deep levels are filled and therefore inactive. Thus, the mobility and trapping times of the carriers increase significantly, producing much faster output signals and higher collected charge. The cryogenic operation of heavily irradiated silicon detectors leads then to a significant recovery of the CCE [69, 70].

In forward-biased mode of a Current Injected Detector (CID), the electric field is controlled by charge injection, i.e. charge is trapped in a radiation-induced defect but not detrapped at a low $T \approx -50^\circ$ C.

The injected carriers are trapped by the deep levels of silicon energy gap reducing the absolute value of effective doping concentration $|N_{\text{eff}}|$, i.e. the space charge density. This changes the electric field distribution by making it continuous through the entire detector bulk, increasing from the injecting contact as $E(x) \sim \sqrt{x}$ and having a maximum at the opposite contact.

The detector is fully depleted regardless of the applied voltage and since the electric field profile is independent of the material properties, no sensitivity to irradiation fluence is expected. However, limited by the space charge, the optimal injected current needs to be adjusted to a certain fluence and increased with the fluence accumulation. Also, the injected current needed for the electric field stabilization

depends on temperature since the steady state density (balance between trapping and detrapping) of the trapped charge is temperature dependent [71, 72, 73].

The main disadvantage of the low temperature operation of tracking detectors is the difficult implementation of a large-scale cryogenic tracker system [56].

3.3 Simulated radiation damage in silicon strip sensors

Charge Collection Efficiency (CCE) can be considered as one of the essential properties to determine the radiation hardness of a silicon detector. From the evolution of CCE with fluence, it is possible to directly observe the effect of the radiation-induced defects on the ability of the detector to collect charge carriers generated by the traversing minimum ionizing particles. Also, understanding the factors that influence its observed position dependence CCE(x) will lead to a more complete interpretation of the degradation of CCE with fluence. Hence, the accurate reproduction and prediction of CCE and CCE(x) by simulations can be a valuable tool in the R&D of radiation hard sensors.

For segmented detectors with various configurations and dimensions, the electric field profile becomes more complicated than in diodes. For efficient charge collection, the electric field maximum produced by the applied bias voltage must be located in the position of the weighting field maximum, i.e. at the segmented electrode. Although the weighting field is the same for equal segmentation geometry, various electric field profiles in irradiated strip detectors (e.g. p-on-n, n-on-p, n-on-n) will lead to differences in charge collection. By optimizing the electric field distribution, fast, reliable and efficient detector operation can be ensured. Thus, the knowledge of the electric field distribution is important for the prediction of the detector operation in harsh radiation environment [74].

Since the electric fields inside the detector cannot be measured directly, the TCAD simulations are an invaluable tool in their study. When calibrated with the indirect electric field information from the edge-TCT measurements, the TCAD simulations offer the possibility to reliably study and predict the evolution of the electric field profiles, both in the bulk and between the segmented electrodes, along with breakdown behavior as a function of the parameter of choice (e.g. voltage, fluence, doping, interface charge density, geometry, etc.).

3.3.1 Implementation of defects to simulation

The quantity of the observed defect levels discussed in section 3.1 set up a vast parameter space that is neither practical nor purposeful to model and tune. Thus, a minimized set of defects constituting an effective defect model is the most meaningful approach for the simulations of irradiated silicon detectors.

Before any implementation of radiation-induced defects to the simulation can take place, the performance of the simulations before irradiation are evaluated comparing the results of the simulation to the corresponding laboratory measurements performed under equivalent conditions. This allows the tuning of the basic simulation parameters as well as the systematic investigation of geometry and process parameter effects [57].

The information of the measured defect properties discussed in section 3.1 is used as a starting point for the device simulations. The simulation of radiation damage in the silicon bulk is based on the effective midgap levels (a deep acceptor and a deep donor level with activation energies $E_{\mathrm{a}} = E_{\mathrm{c}}$ - (0.525 $\pm$ 0.025) eV and E_{v} + 0.48 eV, respectively). The model was first proposed in 2001 by Eremin, Verbitskaya & Li, and entitled later as the "PTI model" (also "EVL model") [5, 6, 75]. The main idea of the model is that the two peaks in the electric field profile $E(z)$ of both proton and neutron irradiated detectors can be explained via the interaction of the carriers from the bulk generated current simultaneously with both electron and hole traps. The physical explanation behind all later models is the same combination of the hole and electron traps.

Simulation by a custom-made software of a 1D diode structure presented in figure 3.1 shows the double peak formation and its dependence on the current generating level. Since the PTI model, basically a three trap model with the two deep traps used to create additional space charges and the third middle level to generate leakage current only, was not designed for TCAD simulation packages, its adaptation to TCAD is not straightforward. To avoid the artificial trap level which generates exclusively leakage current and to account for the experimentally measured leakage current, modifications for the implementation of the defect model to the Synopsys Sentaurus package is required.

In the TCAD simulation packages, the leakage current can be generated either via tuning the charge carrier lifetimes or by introducing defect levels for the non-irradiated and irradiated sensors, respectively. In addition to the leakage current, the lifetime tuning affects also the charge collection via modified trapping in the bulk while the defect levels simultaneously affect the space charge and trapping. Thus, to build a

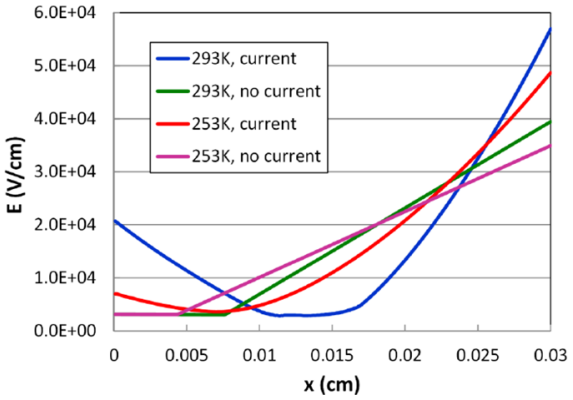

Figure 3.1: The dependence of the simulated electric field profile in the Si bulk on the current generating level of the PTI model. The 300 μm thick 1D diode structure was set to irradiation fluence of 1×10^{15} $\mathrm{n_{eq}cm^{-2}}$ at $V = 500$ V. The double peak formation is observed only when the two midgap levels are supplemented by the current generating level [76].

TCAD defect model on the base of the PTI model with the same two deep levels as those used for the double peak $E(z)$ explanation, all their parameters have to be determined in agreement with experimental data to correctly describe leakage current I_{leak} (as given by equation 3.1), full depletion voltage V_{fd}, transient pulses and CCE after irradiation.

The tuning procedure for the Synopsys Sentaurus defect models, producing bulk properties quantitatively matching the measurements, is described in detail in references [7,57]. To give a general idea of the process flow, the tuning is realized by first applying parametrization of the generated current at fixed $T = 253$ K. Next, the C-V curves are tuned to match experimental results by iterating the ratio of donor concentration to acceptor concentration. Finally, by tuning the acceptor and donor capture cross sections, the transient current curves are adjusted to match the measured signals, shown in figure 3.2a. This is necessary for the simulated CCE to reflect trapping in a real irradiated detector. By repeating the procedure at several fluences leads then to the parametrization of the defect concentrations as a function of fluence.

In the innermost volume of the LHC the most damage producing particles are the pions. The protons have a damage production rate in silicon closest to the pions. Since the high fluence irradiations of protons are much easier to conduct, radiation hardness studies are typically carried out using protons and reactor neutrons [77] to account for the mixture of different particles in the experiment. Hence, the tuning of the Sentaurus bulk defect models was done using data of proton and neutron irradiated

Table 3.1: The parameters of the proton model for Synopsys Sentaurus [7, 57]. $E_{\mathrm{c,v}}$ are the conduction band and valence band energies, $\sigma_{\mathrm{e,h}}$ are the electron and hole trapping cross sections and Φ is the fluence.

Defect type	**Level** [eV]	$\sigma_{\mathbf{e,h}}$ [cm^2]	**Concentration** [cm^{-3}]
Deep acceptor	$E_{\mathrm{c}} - 0.525$	1×10^{-14}	$1.189 \times \Phi + 6.454 \times 10^{13}$
Deep donor	$E_{\mathrm{v}} + 0.48$	1×10^{-14}	$5.598 \times \Phi - 3.959 \times 10^{14}$

detectors. The significant difference in measured $V_{\mathrm{fd}}(\Phi_{\mathrm{eq}})$ for proton and neutron irradiated detectors requires exclusive defect models for each radiation type.

First introduced by R. Eber in 2013 [7] the models, namely the proton model and neutron model (parameters presented in tables 3.1 and 3.2), are valid for fluences from 10^{14} to $\sim 1.5 \times 10^{15}$ $\mathrm{n_{eq}cm^{-2}}$ expected for the strip sensors with different radii in the CMS Tracker at the end of the high luminosity phase of the LHC.

The reliability of the simulated electric field distributions can be confirmed by comparing the measured and simulated transient current curves and collected charges from surface (TCT) and side-plane (edge-TCT) charge injections. The former method is presented in the two plots in figure 3.2 where after red laser front surface illumination the resulting carrier drift in the double peak (DP) electric field is reflected by a DP in the transient signal. Figure 3.3a depicts the collected charges in a neutron irradiated 300 μm thick n-on-p strip detector after infrared laser injections from the side-plane of the sensor at various depths, i.e. an edge-TCT simulation. Both the relative peak values of the collected charges between voltages and the extension of the depletion region (high collected charges), especially for the higher voltages, are in agreement with the measurements in reference [78]. As also the DP formation observed in the measurement is reproduced by the simulation, the electric field distributions in figure 3.3b can be considered to model the real sensor reliably.

As shown in figure 3.4, the simulated CCE of a 300 and 200 μm active thickness sensors compares well to the measured data from both neutron and proton irradiated strip detectors (papers **I, IV**), [7, 57]. At this stage the surface damage was approximated in the simulation by placing a fixed charge density Q_{f} (also N_{f} [79]) at the SiO_2/Si interface. However, to maintain strip isolation in the proton model simulation, it was found that the maximal Q_{f} values had to be limited to considerably lower than expected for a real sensor at the highest investigated fluences ($1 - 2 \times 10^{12}$ cm^{-2} [46], [80]). At the studied fluence range the strips in the real sensors remain isolated.

Table 3.2: The parameters of the neutron model for Synopsys Sentaurus [7, 57]. Symbols are as in table 3.1.

Defect type	**Level** [eV]	$\sigma_{\mathbf{e,h}}$ [cm^2]	**Concentration** [cm^{-3}]
Deep acceptor	$E_\mathrm{c} - 0.525$	1.2×10^{-14}	$1.55 \times \Phi$
Deep donor	$E_\mathrm{v} + 0.48$	1.2×10^{-14}	$1.395 \times \Phi$

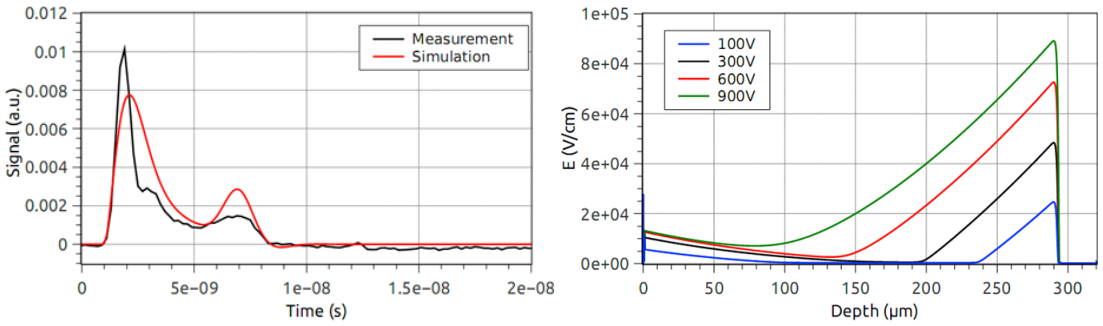

(a) (b)

Figure 3.2: (a) Measured and Sentaurus proton model simulated transient signals in a 300 μm thick pad detector irradiated by the fluence of $1 \times 10^{15}\mathrm{n_{eq}cm^{-2}}$ at $V = 400$ V. (b) Corresponding simulated electric field profiles in the detector bulk for varying bias voltages [7].

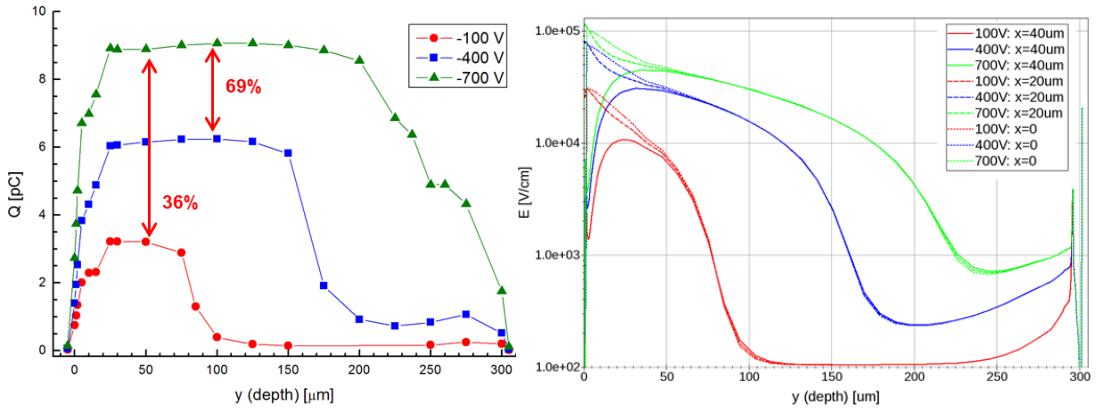

(a) (b)

Figure 3.3: (a) Edge-TCT simulation using the Sentaurus neutron model with detector parameters matched to a measurement by G. Kramberger et al. [78] of a neutron irradiated 300 μm thick n-on-p strip detector at the fluence of 5×10^{14} cm^{-2} [57]. Corresponding measured ratios of the peak collected charges were ~33% and ~71%. (b) Corresponding electric field distributions in the Si bulk with cuts made from the center of the strip ($x = 0$) to the center of the interstrip gap ($x = 40$ μm).

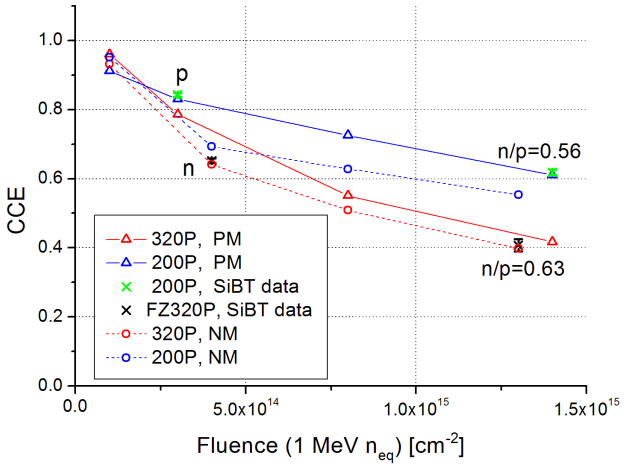

Figure 3.4: Measured and simulated CCE(Φ_{eq}) for the n-on-p strip sensors with a strip pitch of 120 μm (paper **I**). Types of irradiation are marked in the plot as p = proton, n = neutron and n/p = mixed fluence with the ratios of the particles indicated. PM = proton model, NM = neutron model and e.g. 200P is a p-type sensor with a 200 μm active region thickness. The experimental data was measured with the SiBT set-up [81, 82].

3.4 Simulation Framework

Sentaurus TCAD is a commercial simulation software package produced by Synopsys. Designed to simulate semiconductor technology for various applications, it offers a variety of options to design silicon devices as well as several models to simulate silicon sensors under operational conditions. These include the basic analysis of the leakage current, the AC small signal analysis and the transient analysis for the time evolution of signals generated by charge injections of multiple options (lasers, MIPs, alphas, etc.).

3.4.1 Simulation flow

A straightforward way to apply the simulation package is to manage the simulation runs and results analysis with a Sentaurus Workbench tool. Several tools are run in succession to first generate the device structure to be modeled (Sentaurus Structure/Device Editor), then to carry out the actual physics simulation (Sentaurus Device) and finally to analyze the results (Inspect/Sentaurus Visual). Also a processing step

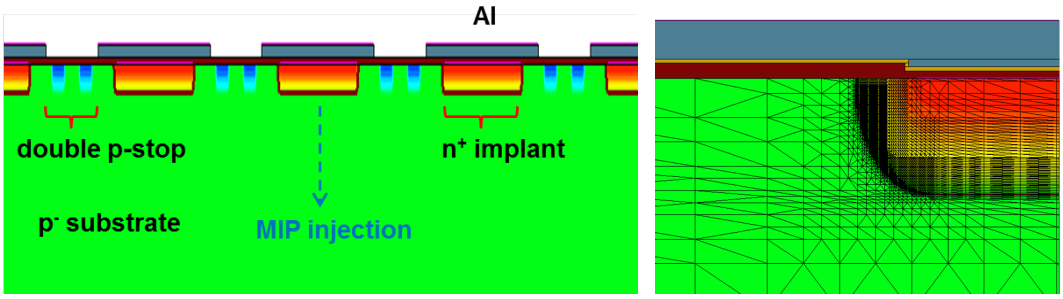

(a) (b)

Figure 3.5: (a) The front surface of a 2D-designed n-on-p sensor structure with a double p-stop strip isolation (not to scale). Charge injection position for the CCE simulations in figure 3.4 is also illustrated. (b) Close-up of the strip implantation and metallization. The Al layer with a via-structure is in grey while the nitride and oxide layers are in light brown and dark brown, respectively. The meshing is reduced at the high doping gradient of the strip implant to produce its profile accurately.

for the doping implantations is possible. Minimum number of input files required for a succesful simulation include the device structure file, the physics parameter file, the simulation command file and the analysis file.

The parameter values under investigation are given as an input from the Workbench to the physics command file during the simulation. In this manner, the needed parameter variations can be achieved in a single simulation run.

The device structures can be generated in both 2D or 3D. Sensors that do not have structural variations in the third dimension, i.e. diodes and strip sensors, can be modeled in 2D, shown in figure 3.5, and extended to the dimensions of a real device by an appropriate coefficient. This approach is time and memory efficient because it requires significantly smaller number of mesh points where the physics equations for each point are solved. The 3D device structures, although requiring much computing time and capacity, model reality and are mandatory for reliable simulations of the pixel and 3D columnar sensors, presented in figure 3.6.

Compact descriptions of the physics models, boundary conditions and the role of grid size optimization in the simulation process are given in the appendix A.

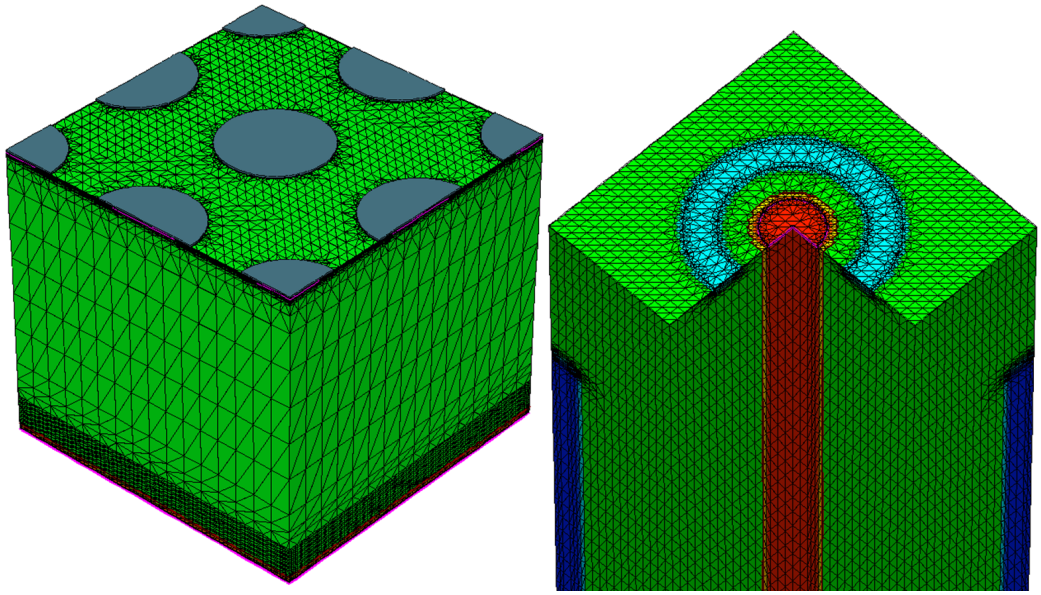

(a) (b)

Figure 3.6: Sensor structures designed in 3D. (a) A 100 μm thick p-on-p pixel sensor with a 55 μm pitch. The field oxide has been stripped for a view of the meshing. (b) Sliced view of a double column-double sided 3D n-on-p sensor with a p-stop isolation. Aluminum and oxide have been stripped from the surface.

Chapter 4

Results

The TCAD simulations in the following sections 4.1 and 4.2 applied p-type bulk material with $\langle 1,0,0 \rangle$ crystal orientation. The modeled irradiations were always considered in 1 MeV neutron equivalent fluences ($\mathrm{n_{eq}cm^{-2}}$).

4.1 Simulation model for surface and bulk damage in silicon strip detectors

Investigation of the TCAD bulk damage models in segmented devices with surface damage modeled by Si/SiO_2 interface charge density Q_f has revealed that the approach is not sufficient to reproduce the observed surface properties of irradiated detectors. As discussed at the end of the section 3.3.1, the strips became shorted at high proton fluences when they were expected to be isolated by the experiment. Simultaneously the resulting interstrip capacitances C_{int} remained several orders of magnitude above the geometrical values expected from the measurements. Additionally, the observed position dependence of CCE in irradiated strip detectors [47,48], i.e. CCE(x), was not reproduced at a lower fluence of 3×10^{14} $\mathrm{n_{eq}cm^{-2}}$. Thus, these observations represented a further demand for the parameter tuning of the defect models for segmented sensors. This has been realized by implementing additional traps N_{it} at the SiO_2/Si interface (Silvaco Atlas [83]) or extending from the interface with a wider depth distribution (Sentaurus papers **I**, **II**, [57]). Before these two approaches, no studies on the modeling of combined bulk and surface damage in segmented sensors had been published.

Earlier published simulation studies for surface damage exclusively have modeled damage by either interface charge density Q_f [84,85] (as in section 3.3.1), by including in the threshold voltage expression the induced flat-band voltage shift [86], or by

three interface traps with parameters matching the measurements of X-ray irradiated devices [45].

In the Silvaco Atlas TCAD model [83], it is assumed that for a given interface trap density N_{it} 60% are deep acceptor traps (E_{c} - 0.60 eV) and 40% shallow acceptor traps (E_{c} - 0.39 eV). Since the measured Q_{f} and N_{it} values [46] are similar in magnitude, N_{it} was set to a value equal to Q_{f} for the simulations. Complemented by the 2-defect bulk model with experimentally matching properties, the combined bulk & surface damage model reproduces interstrip resistances R_{int} in very close agreement with the measurements.

The inherent differences between the standard parameter sets of the two TCAD simulation frameworks used throughout the HEP community, Synopsys Sentaurus and Silvaco Atlas, have been shown to produce results that are decisively different from one another [7]. Therefore, to produce equal results of irradiated sensors, the same parameter values cannot be used in the defect models of the two packages.

When the N_{it} approach was applied with the Sentaurus proton model, it was found that the expected C_{int} values were not reproduced [87] at the Q_{f} range where CCE(x) was matching the measurement. By applying a deeper distribution for the surface traps, namely 2 μm from the Si/SiO_2 interface, it was possible to reach agreement with the measurement for the aforementioned surface properties and maintain strip isolation also at high proton fluences, while leaving the bulk properties of the proton model unaffected (papers **I**, **II**). Comparison with the proton model, presented in figure 4.1a, shows the effect of the shallow acceptor traps resulting in a five orders of magnitude decrease in the electron density at the interstrip region. It should be emphasized that the depth distribution of the applied single shallow acceptor level (E_{c} - 0.40 eV) is concentration dependent and other values could be used to same effect.

For the CCE simulations, the charge injection position was fixed in the middle of the centermost strip, shown in figure 3.5a. For the CCE(x) simulations the position was varied from the midgap between the strips to the center of the strip, presented in figure 4.1b. This plot also provides information on the strip isolation; when the strips are isolated, the cluster CCE (total collected charge in the sensor compared to the corresponding charge in a non-irradiated sensor) decreases towards the midgap but when shorted the cluster CCE becomes position independent. The cluster CCE loss (comparison of the collected charges after injections at the midgap between the strips and at the center of the strip) between the strips was then tuned to find agreement with the measured values by scanning the interface charge density values, illustrated

Table 4.1: Parameters of the shallow acceptor level included in the non-uniform 3-level model for Synopsys Sentaurus (paper **I**), parametrized for the fluence range $(0.3 - 1.5) \times 10^{15}$ $\mathrm{n_{eq}cm^{-2}}$. Symbols are as in table 3.1.

Defect type	**Level** [eV]	σ_e [$\mathrm{cm^2}$]	σ_h [$\mathrm{cm^2}$]	**Concentration** [$\mathrm{cm^{-3}}$]
Shallow acceptor	$E_\mathrm{c} - 0.40$	$8{\times}10^{-15}$	$2{\times}10^{-14}$	$14.417{\times}\Phi{+}3.168{\times}10^{16}$

in figure 4.2.

The test beam measured average cluster CCE loss between the strips [47] in the 200 μm active thickness Fz and MCz sensors with 120 μm pitch and p-spray and p-stop isolations was reproduced by the simulation when the $Q_\mathrm{f} = (8.5 \pm 1.0) \times 10^{11}$ $\mathrm{cm^{-2}}$ and $(1.6 \pm 0.2) \times 10^{12}$ $\mathrm{cm^{-2}}$ on the left and right sides of figure 4.2, respectively.

The simulated interstrip capacitance C_int results, presented in figure 4.3, offer a further tool to cross-check the functionality of the model. Since the geometrical capacitance of $\sim$1.8 pF is expected at 0 V for both fluences, figure 4.3a shows that all corresponding values of Q_f determined by the CCE(x) simulations in figure 4.2a are acceptable with respect to C_int. The corresponding plots for the higher fluence on both figures display that the agreeable values are now limited by C_int to $Q_\mathrm{f} < 1.42 \times 10^{12}$ $\mathrm{cm^{-2}}$.

Simulated CCE(x) was found to be dependent on the shallow acceptor concentration in the 3-level defect model and on Q_f at a given fluence. Thus, by fixing one it is possible to parametrize the other as a function of fluence. Due to shortage of exact measured data of Q_f, estimated values were used, against which the shallow acceptor concentration was tuned. Hence, at this stage the approach provides more a method than exact quantitative information with regard to these properties. With the existing measured CCE(x) data, a preliminary parametrization, presented in table 4.1, of the 'non-uniform 3-level model' was performed for fluences from 3×10^{14} to 1.4×10^{15} $\mathrm{n_{eq}cm^{-2}}$ for the strip pitch of 120 μm (paper **I**). The observed behavior is further analyzed and discussed in chapter 5.

4.2 Simulation study of a thin p-on-p pixel detector

The initial motivation for this research was to understand the factors that led to the significantly lower charge collection in the thin p-on-p pixel sensor than in its p-on-n counterpart at a depletion voltage range of 15–100 V (paper **V**). The collected charges

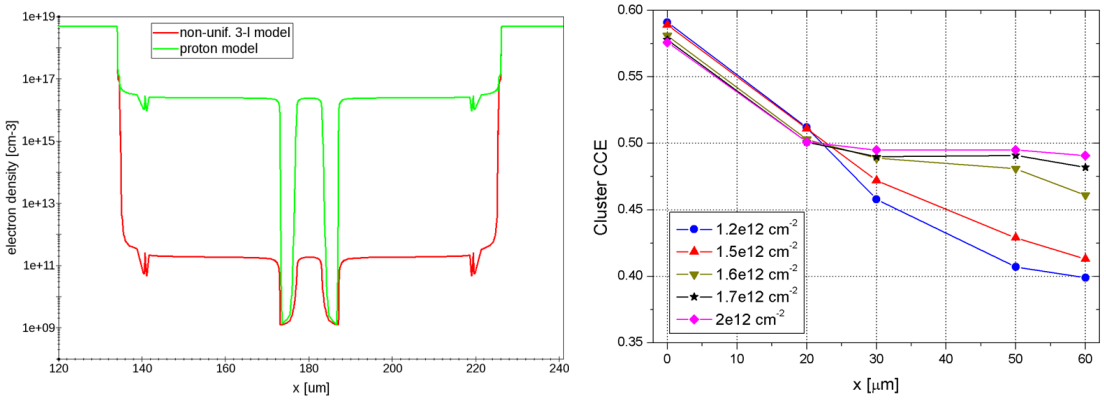

(a) (b)

Figure 4.1: Simulation results of a 200 μm active thickness n-on-p strip sensor with a 120 μm pitch using the non-uniform 3-level defect model after irradiation to 1.5×10^{15} $\mathrm{n_{eq}cm^{-2}}$. (a) Comparison of electron density results with the proton model for $Q_\mathrm{f} = 1.2 \times 10^{12}$ $\mathrm{cm^{-2}}$. The cut was made at 50 nm below oxide between the $\mathrm{n^+}$ strips. Positions of the double p-stops can be observed in the center of the plot, where both concentrations reach their respective minima (paper **II**). (b) Simulated CCE(x) at V = -1 kV. Charge injection positions x = 0, 60 μm correspond to the center of the strip and the center of the interstrip gap, respectively. Varying the values of Q_f displays the evolution of the CCE loss between the strips.

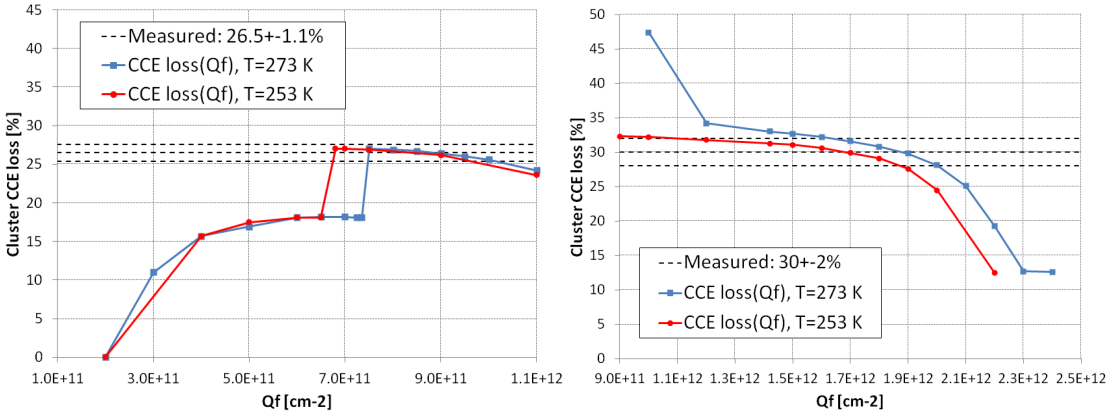

(a) (b)

Figure 4.2: Measured [47] and simulated CCE loss of a 200 μm active thickness n-on-p strip sensor with a 120 μm pitch using the non-uniform 3-level defect model at T = 263±10 K and V = -1 kV (paper **I**). (a) $\Phi_\mathrm{eq} = 3 \times 10^{14}$ $\mathrm{cm^{-2}}$. Measured detectors were proton irradiated. (b) $\Phi_\mathrm{eq} = 1.4 \times 10^{15}$ $\mathrm{cm^{-2}}$. Measured detectors were irradiated by mixed fluences $\Phi_\mathrm{eq} = (1.4 \pm 0.1) \times 10^{15}$ $\mathrm{cm^{-2}}$ with relative fractions $\mathrm{n/p} = 0.60 \pm 0.04$.

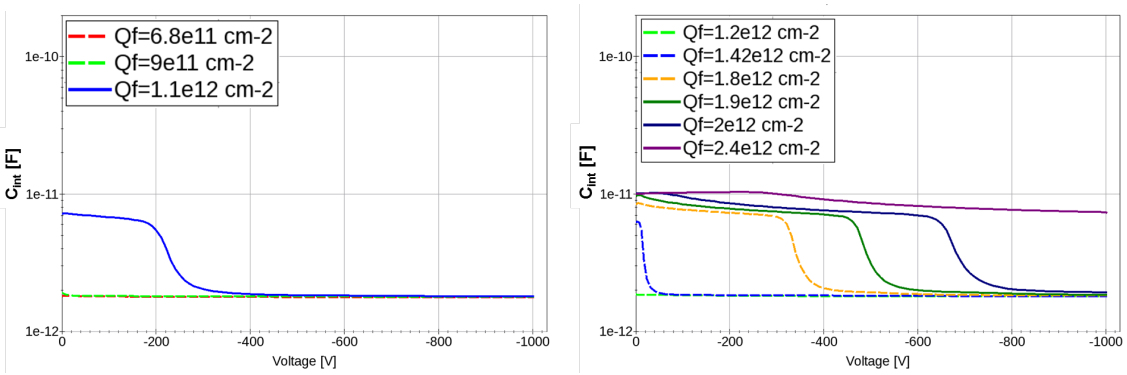

(a) (b)

Figure 4.3: Corresponding simulated interstrip capacitances C_{int} for the sensor and fluences in figure 4.2 at $T = 253$ K. The dashed curves indicate the Q_{f} values where the simulated CCE loss between the strips matches the measurement. The values of C_{int} were determined by the method described in [88]. (a) $\Phi_{\text{eq}} = 3 \times 10^{14}$ cm^{-2}. (b) $\Phi_{\text{eq}} = 1.4 \times 10^{15}$ cm^{-2}.

were injected by a keV energy range proton beam from the sensor backplane.

4.2.1 Simulation set-up

For the comparative simulation study of the electrical characteristics and charge collection behaviour in the voltage range 0–100 V of the p-on-p and p-on-n thin pixel sensors, the 3D-structure presented in figure 4.4 was applied. This was deemed necessary since a 2D-structure accounts only for the interactions between a single column of pixels. Also, the correct reproduction of the local electric fields at the circular shaped pixels required a 3D-structure.

The simulated pixel sensor configurations replicated the design parameters of the real sensors as closely as possible and had a 100 μm thickness, a 55 μm pitch and a pixel implant diameter of 30 μm with the resistivities of $\sim$10 k$\Omega \cdot$ cm and $\sim$5 k$\Omega \cdot$ cm, respectively. The aluminum metallizations above the pixel implants and their vias through the oxide layer for the DC-coupled contacts are detailed in the cross-sectional slice presented in figure 4.4b.

4.2.2 Electrical characteristics

The simulated C-V characteristics agreed within 10% in terms of the full depletion voltage with the measurements in reference [89]. The results are different for the two

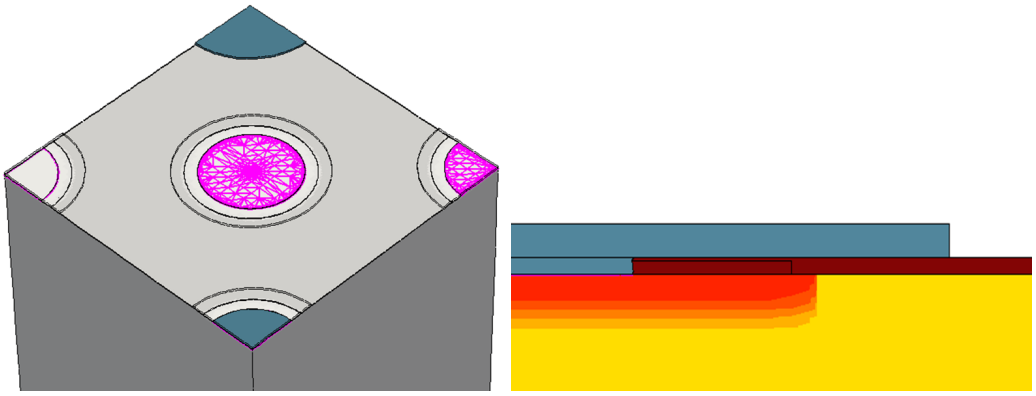

(a) (b)

Figure 4.4: (a) A 3D-design of a pixel sensor front surface structure of 5 pixels with the field oxide layer stripped. The magenta mesh regions at the center and rightmost pixels highlight the positions of the DC-coupled contacts. The gray layers on the top and bottom corners are the pixel metallization and via (Al contact to the Si through the oxide layer) structures, respectively. Black contour lines around the four pixels illustrate the edge of the stripped aluminum overhang. Pixel implants are in white while the Si bulk is in light gray. The n^+ layer and the metallization of the non-segmented backplane are not pictured. (b) Cross-sectional view of the simulated pixel implant and its metallization. Topmost is the gray aluminum layer with a via-structure through the brown oxide layer. Below these the heavily doped implant region is in red while the surrounding lightly doped Si is in yellow.

sensor types because the depletion starts in the p-on-p from the non-segmented side with an immediate increase of the depletion depth at small voltages, while for p-on-n it starts from the segmented side, for which part of the voltage is used to deplete the area between the pixels, slowing the extension of the effective depletion depth and the change of capacitance, as presented in figures 4.5a and 4.6.

Figure 4.6 also shows that the depletion process of the p-on-p sensor is further enhanced by the extension of the electric field from the electrode sides due to the potential differences produced by the high doping gradients at the pixel edges. This is reflected in figure 4.5a where around 6 V the rate of the bulk depletion changes from equal to the p-on-n sensor to almost instantaneous. In figure 4.7 it is shown that at higher values of the reverse bias voltage, the electric field maximum in the p-on-p sensor is at the pixel side, thus good resolution and low collection times can be expected.

As can be seen from figures 4.6 and 4.7, the peak electric fields at the pixels are higher in the p-on-n sensor, especially at lower voltages. This would lead one to expect generally better breakdown behaviour for the p-on-p sensor. However, as presented in figure 4.8, the rapid increase of the electric fields with voltage at the pixel edges in the p-on-p sensor eventually leads to a breakdown voltage that is very close the p-on-n sensor. To reproduce the measured leakage current that was roughly three times higher in the p-on-n sensor [89], the carrier lifetimes were tuned.

The interpixel resistance simulations in figure 4.5b display over three orders of magnitude higher resistance for the p-on-n sensor until full depletion is reached in the p-on-p sensor. With the V_{fd} result from figure 4.5a it can be seen from the R_{int} curve of the p-on-p sensor that after the bulk is fully depleted it still requires $\sim$2 V to deplete the inter-pixel region. After $\sim$9 V, the pixel isolation between the two sensors is identical. Thus, no significant differences in charge collection due to the electric field distribution and the interpixel isolation in the two sensor types can be expected after about 9 V of bias voltage.

4.2.3 Charge collection

Since the measured charge was recorded from a single pixel using a trigger that excluded all two pixel or larger cluster events, the chosen charge injection position at the center of the sensor's non-segmented backplane for the simulation was considered to give sufficient approximation of the real measurement situation.

The initial charge collection simulations with the charge carrier lifetimes tuned to

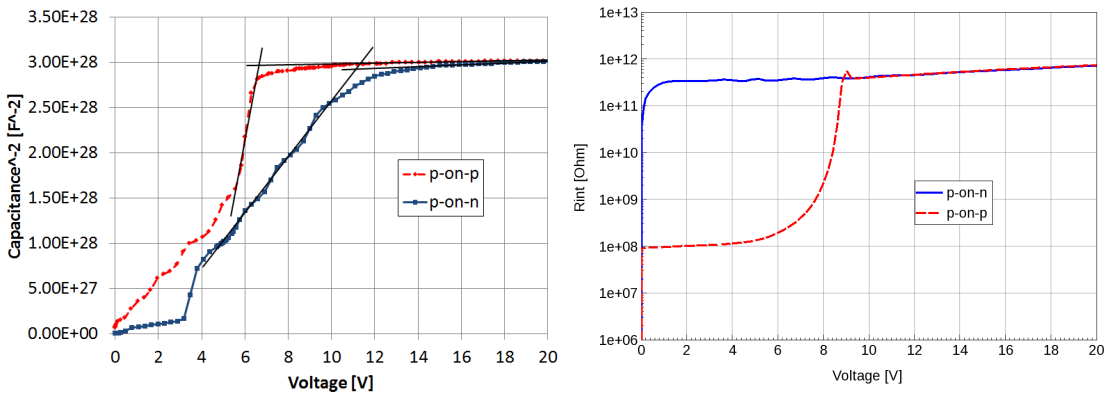

(a) (b)

Figure 4.5: (a) Simulated C-V curves for the two sensor types and their V_{fd} determined from the crossing point of the linear fits to the dynamic and plateau regions of the curves. (b) Interpixel resistances R_{int} as a function of bias voltage for the two sensors.

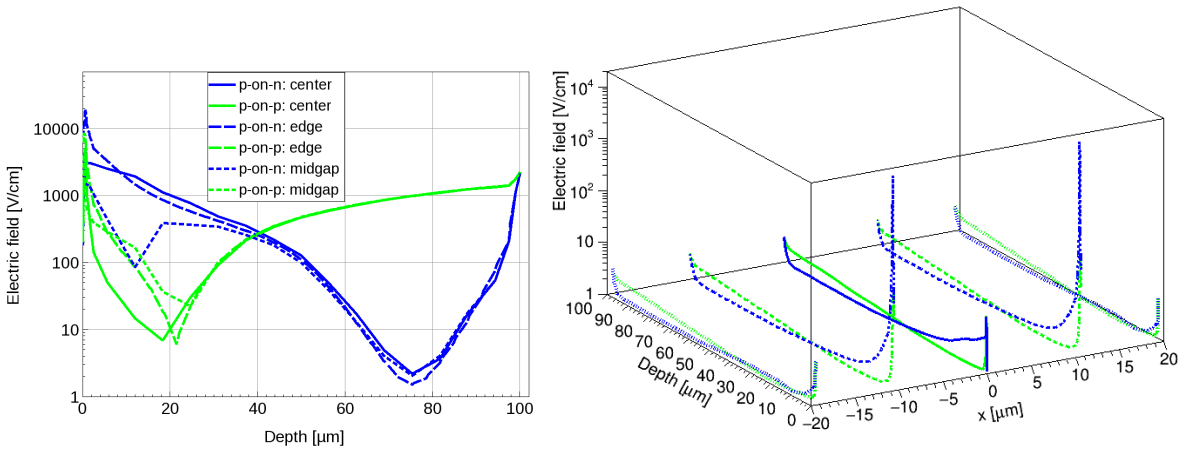

(a) (b)

Figure 4.6: (a) Simulated electric field distributions through the bulk of the two sensor types at the lower part ($V = 5$ V) of the investigated voltage range. The cuts were made in the middle of the centermost pixel (center), at the pixel implant edge (edge) and at the center of the interpixel gap (midgap). The ratio of the electric field maxima E(p-on-p)/E(p-on-n) at the pixel edge is ∼43%. (b) A 3D view displaying the spatial distribution of the electric field cuts in (a).

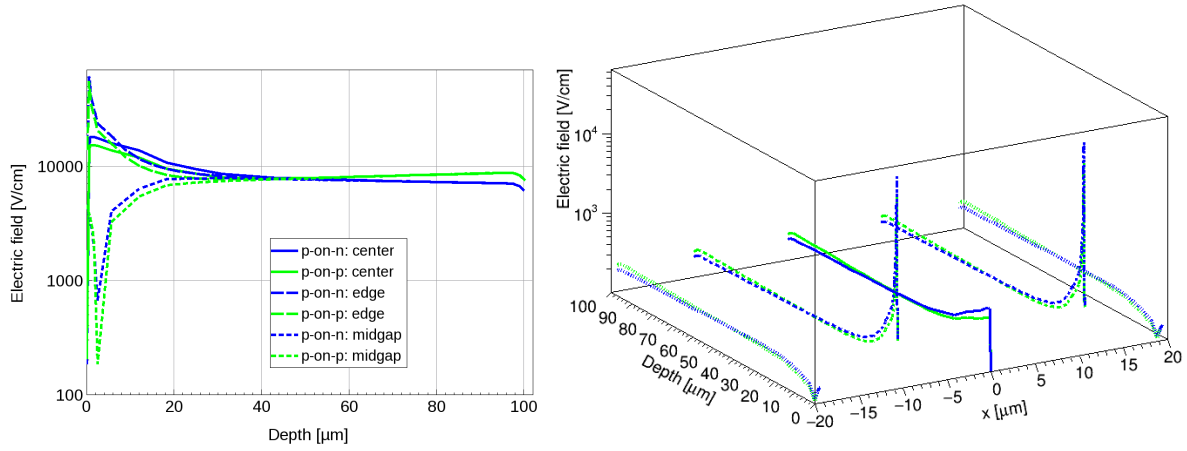

(a) (b)

Figure 4.7: Simulated electric field distributions through the bulk of the two sensor types at the higher part ($V = 90$ V) of the investigated voltage range. The cuts were made as in figure 4.6a. The ratio of the electric field maxima E(p-on-p)/E(p-on-n) at the pixel edge is ∼87%. (b) A 3D view displaying the spatial distribution of the electric field cuts in (a).

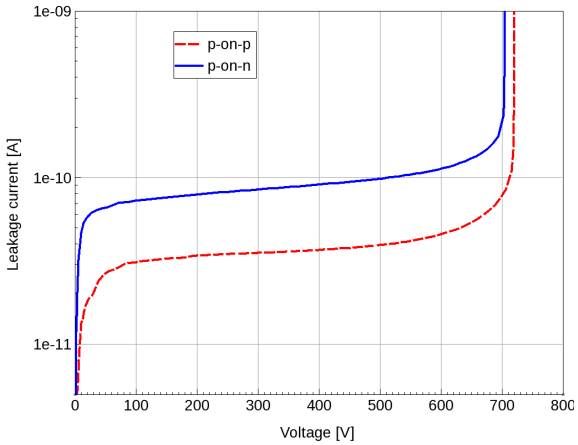

Figure 4.8: Simulated I-V curves for the two sensor types and their breakdown voltages V_{bd}. The V_{bd} is ∼16 V lower for the p-on-n sensor.

reproduce the experimentally observed difference in the leakage current (presented in figure 4.8) displayed similar qualitative behaviour with the measured curves in (**V**). As seen in figures 4.9 and 4.10a, the p-on-n sensor collects higher charges at low voltages and at higher voltages the collected charges in the two sensors converge. However, at e.g. 20 V the measured collected charge was ∼25% higher in the p-on-n sensor, yet the corresponding difference was only ∼5% in the simulation. Also, the initial collected charges for both sensors around 15 V are considerably higher than in the measurement. Any effect from the charge sharing in the measurement was ruled out by the charge collection conditions described above. Also, the interpixel resistance simulations in section 4.2.2 displayed an identical pixel isolation in the two sensor types after ∼10 V. Thus, the differences in this regard between simulation and measurement could not be considered to explain the smaller difference in the simulated collected charges between the two sensor types. In addition, since the backplane metallization thicknesses and doping diffusion depths were essentially identical in the measured sensors, no contribution from different scattering of protons or charge carrier losses at the non-active region could be expected.

Tuning of the carrier lifetimes

Thus, further study of the charge collection was focused on the charge carrier lifetimes in the two sensor types. The initial objective of the carrier lifetime tuning was to reproduce simultaneously lower leakage current and lower charge collection at low voltage for the p-on-p sensor. In the case of a hole dominated transient signal due to the backplane charge injection, this was addressed by increasing the electron lifetimes while decreasing the hole lifetimes with respect to the p-on-n sensor. The effect of the tuning for the carrier collection is seen in figure 4.9 where the differences between the two sensor types in electron (small t) and hole (larger t) contribution to the current signal are clearly visible.

By decreasing the lifetimes of both carrier types, it is possible to significantly shift the charge collection evolution with voltage towards the measured values in the p-on-p sensor, as displayed by the solid red curve (p-on-$p_{Q_{coll}}$) in figure 4.10a. The ratio of the collected charges by the 800 keV proton injection in the two sensors at 15 V now matches the measurement, while the collected charge relative to the maximum collection is within 10% of the measured p-on-p sensor. The crossing point of the two curves is now only ∼10 V from the measured and at voltages beyond the crossing point the p-on-p collects somewhat higher charges than p-on-n as was also seen in the

measurement. Thus, this gives an indication that higher trapping rate of holes in the p-bulk at low voltages leads to the observed charge collection difference in the two sensors. At increased bias voltages, the total drift time of the carriers is reduced due to the higher electric field leading to reduced number of trapped carriers and higher collected charges [31].

Applying this approach also to the p-on-n sensor would provide a means to tune the low voltage charge collection along with the charge collection and leakage current ratios between the two sensors close to measured values. However, even though the mutual ratio of the leakage current in the sensors would be preserved, its absolute values would increase beyond measured values in the process. Thus, the tuning of the carrier lifetimes should be considered as an effective approach to reach an estimation of the higher hole trapping in the p-on-p sensor that could explain the measured charge collection behaviour. The implementation of specific trap levels, i.e. deep traps with high hole trapping probability and low contribution to the leakage current [35], to the simulation with characteristical properties extracted from measurements would be a more precise approach, but lacking such data, this is left to a later study.

Voltage of complete charge collection

A further simulation study of the voltage required for a complete charge collection (V_{cpl}), presented in figure 4.10b, of injections from the front surface and backplane revealed a strong dependence of V_{cpl} on the charge carrier type and a significant dependence on the size of the generated carrier cloud.

Since only general tendencies were investigated, a simplified p-on-n 2D-structure was applied. Of the four studied charge injections, the IR laser signal (produced by both electrons and holes) is collected at $V_{\mathrm{cpl}} = V_{\mathrm{fd}} \approx 11$ V. When a red laser (absorbed within 10 μm) of equal intensity is injected from the backplane (front surface injection resulted in a curve overlapping the IR laser curve) the signal produced by the hole drift more than doubles V_{cpl}. The 800 keV proton injection generates a considerably higher localized carrier density resulting in V_{cpl} ~15 V from the front surface injection (electron drift) and about three times higher V_{cpl} from the hole drift due to the backplane injection. Thus, regardless of the approximations of the 2D-structure[1] the results show that a transient signal produced by a hole drift (with about three times lower mobility to electrons) leads invariably to V_{cpl} higher than V_{fd}. Additionally, a

[1]Collected charges in figure 4.10b at low voltages are much lower than in the 3D simulations due to the underestimation of the electric field evolution at the pixels.

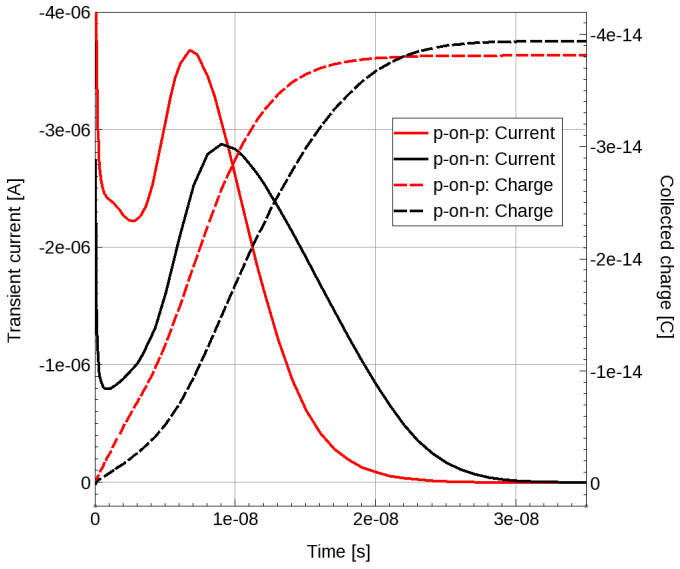

Figure 4.9: Simulated transient currents and collected charges in the p-on-p and p-on-n sensors of figure 4.4 at $V = 23$ V. Charges in the range of a 800 keV proton resulting from a backplane injection and collected at the centermost pixel are plotted. The carrier lifetimes correspond to the tuned leakage current in figure 4.8. The collected charge scales to energy as 4×10^{-14} C $\sim$ 900 keV.

localized carrier density generated by an energy deposition in the range of hundreds of keV results in a decrease of the mobility of the carriers, due to the increase of carrier-carrier interactions, leading to a shift of V_{cpl} to higher voltages. Hence, these two observations provide an interpretation of the measured V_{cpl} behaviour in (paper **V**).

4.3 Simulation study of an epitaxial GaAs p-i-n detector

This study was motivated by the need to verify the characterization measurements of the newly processed detectors with less studied material in (paper **III**) as well as to investigate whether the full simulation characterization, including electrical properties and charge collection, of a GaAs detector can be performed using TCAD.

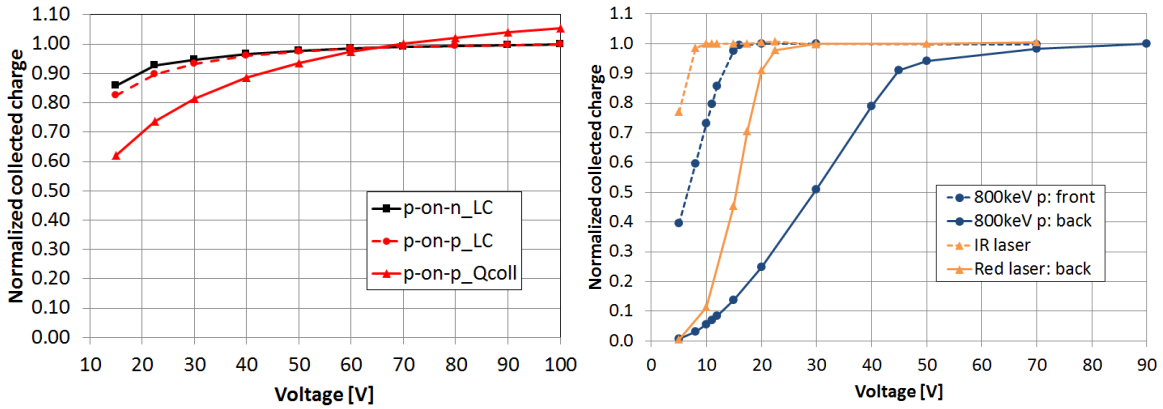

(a) (b)

Figure 4.10: (a) Simulated charges collected at the centermost pixel of the structure in figure 4.4a for p-on-p and p-on-n sensors. Normalization is done to the charge collected by the p-on-n sensor at $V = 100$ V. LC indicates the curves produced by the charge carriers with lifetimes tuned to reproduce experimentally matching leakage current ratio in the two sensors. Q_{coll} corresponds to the carrier lifetime tuning to shift the charge collection behavior closer to the measurement in (paper **V**). (b) Simulated charges collected at the centermost pixel of a 2D three-pixel p-on-n sensor similar to a diagonal slice of the 3D-structure in figure 4.4a. Normalization is done to the maximum charge collected at each injection. Charge injections from the front surface and the backplane are indicated accordingly.

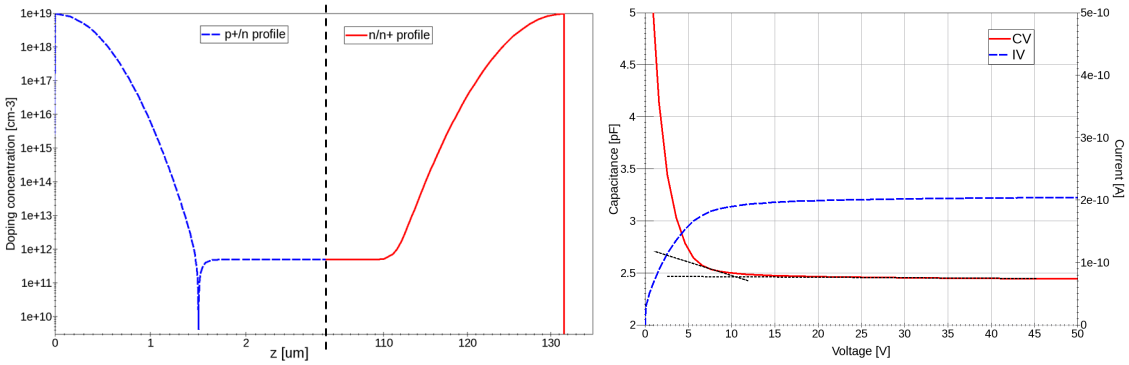

(a) (b)

Figure 4.11: (a) Simulated doping profiles of p^+ and n^+ layers with tuned diffusion depths to create an effective structure similar to the measured GaAs pin-diode described in (paper **III**). (b) Simulated C-V (f = 10 kHz) and I-V curves at T = 300 K for the GaAs diode structure with an active thickness of 110 μm and surface area matching the real diode, along with the observed deep donor level in the epitaxial layer. The geometrical capacitance is ∼2.32 pF while the leakage current density is ∼8.5 nA/cm^2. The full depletion voltage of about 10 V was determined as in figure 4.5a.

4.3.1 Electrical characteristics

The initial simulated GaAs diode structure had the dimensions $A \times 10 \times 131.5$ μm^3, where A is the area factor to match the 2D-structure dimensions with the real diode. The electrical contacts were provided by the DC-coupled Ni contacts on the front and backplanes. Presented in figure 4.11a, the doping profiles of the p^+ and n^+ implantations were tuned to create approximations for the layer thicknesses of the p^+/i/n^+ configuration.

For the modifications of the simulation set-up from the silicon device simulations new parameter files for the GaAs and Ni materials had to be generated and integrated to the main physics command file. To reproduce the measured geometric capacitances, full depletion voltages (∼10 V) and leakage current densities (∼10 nA/cm^2) the deep donor level suggested by the DLTS measurements was implemented to the GaAs epi-layer. The simulations in figure 4.11b reproduced the measurements after the capture cross section and concentration were tuned to $\sigma = 5 \times 10^{-10}$ cm^2 and $N_t = 1.4 \times 10^{12}$ cm^{-3}, respectively. Due to the limited temperature range of the used DLTS set-up the parameters of the observed deep donor level were not unambiguously determined. Therefore, the applied trap level E_V + 0.97 eV should be considered as preliminary.

4.3.2 Transferred electron effect

In GaAs and materials of similar band structure, a negative differential mobility is generated by high driving fields. This effect is caused by the transfer of electrons into an energetically higher side valley with a considerably larger effective mass, i.e. when the electric field in the material reaches a threshold level, the mobility of electrons starts to decrease with increased electric field due to transferred electrons from one valley in the conduction band to another. In the process, the electron effective mass moves from small to large and the mobility decreases from very high to very low [15,16].

For the simulation of the effect, first the charge injection depth was set to ∼3 μm from the device front surface to generate the transient signal essentially from the electron drift. Then the `TransferredElectronEffect` statement was added to the high field saturation definition of the electrons in the mobility section of the physics simulation command file.

As seen in figure 4.12, the simulated transient currents in the GaAs diode at T = 300 K display the macroscopic result of the transferred electron effect, i.e. when the voltage and the resulting electric field in the diode move closer to the values that produce the peak electron drift velocity a reduced collection time t_{coll} is observed. In the GaAs diode with an active thickness of about 110 μm, the voltage producing the maximal velocities is in the range of 37–45 V [15, 90]. Voltages below and above this region will then lead to longer t_{coll}. The simulated transient signal shapes are in line with the observed while the difference in signal heights agrees within 14% with the measurements in (paper **III**).

To reproduce the measured differences in signal amplitude, the simple diode structure described in section 4.3.1 had to be replaced by a wider structure that took into account the lateral expansion of the electric field beyond the diode region. If the lateral expansion of the electric field is not considered the fields for the given voltage will be higher than in the real diode, affecting the drift velocities. For simplicity, the deep donor level was not applied for the transient simulations that were carried out to investigate the transferred electron effect. Hence, the absolute collection times are shorter than those measured.

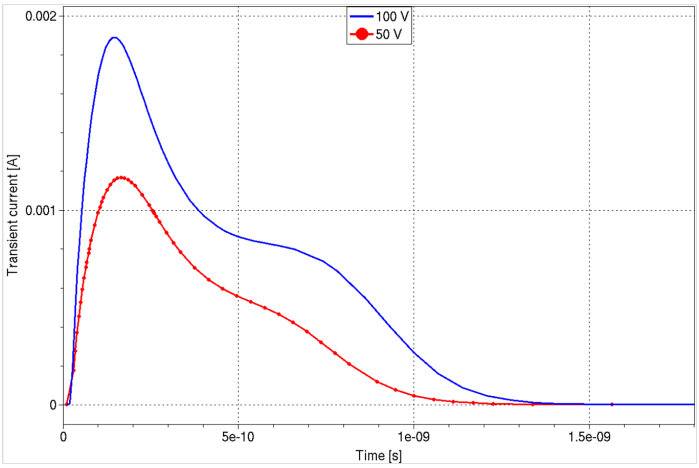

Figure 4.12: Simulated transferred electron effect on transient current in GaAs diode. The shortest t_{coll} is given by the voltage producing a drift velocity closest to the peak value.

Chapter 5

Conclusions and discussion

5.1 Theoretical implications

5.1.1 Interaction of the interface charge density with traps

As discussed at the end of section 4.1, the simulated CCE(x) was observed to be governed by the shallow acceptor concentration close to the sensor surface and the interface charge density Q_{f} at a given fluence. This creates a possibility to parametrize one of these variables as a function of fluence if the other variable can be fixed by measurements.

Since the non-uniform 3-level model can be viewed as the proton bulk model complemented by interface traps N_{it} with 2 μm depth distribution, it can be concluded that the deeper distribution of N_{it} was the only approach from several options investigated[1] that simultaneously reproduced experimentally matching strip isolation, C_{int} and CCE(x) in the Sentaurus TCAD simulations.

The effect of the non-uniform 3-level model to the CCE(x) leads to the interpretation that the acceptor traps close to the surface of the sensor remove both accumulation layer and signal electrons, i.e. the better the radiation damage induced strip isolation, the higher the CCE loss between the strips. Conversely, if the shallow acceptor concentration is kept constant and Q_{f} is increased, more traps are filled leading to increased charge sharing and decreased CCE loss between the strips.

In figure 4.2a, the simulated cluster CCE loss in the low Q_{f} region falls below the experimentally observed values. This is due to increased opposite sign contribution to

[1]The investigated alternatives (e.g. uniform distribution throughout the bulk, confinement strictly to the Si/SiO_2 interface, etc.) are elaborated in reference [87] and (paper **II**).

the cluster charge from strips further away from the position of the charge injection. When Q_f is set to a small value, the number of electrons attracted to the Si/SiO_2 interface is significantly reduced. This leads to vast increase of the negative space charge, produced by the acceptor levels in the isolation implantations and the defect model close to the surface for the given fluence, due to the lack of compensation from the electrons in the accumulation layer.

Thus, when the charge is injected from the middle of the centermost strip in figure 5.1, the center strip collects a positive charge from the signal electrons while the two adjacent strips collect a negative charge that is generated by the movement of the holes along the surface repulsed by the injected signal holes [91]. Charge sharing from the signal carriers is minimal due to the domination of the acceptor states. Due to the opposite velocity vector to both signal charge carriers along with opposite charge to electrons, the induced current from the drift of the surface holes is necessarily of an opposite sign to the signal current. This conforms with the Shockley-Ramo Theory, where the induced current is proportional to the velocity vector and the charge of the drifting carrier, $I \propto q\vec{v}$, where $q = \pm e$ with e as elementary charge.

When the charge is injected at the center of the interstrip gap in this situation, the effect of hole current along the surface is confined between the two n^+ strips closest to the injection point and both collect a positive signal reduced by the trapping. Hence, as seen from the reduced CCE loss in figure 4.2a, the cluster charge collected from the injection at the center of the strip moves closer to the corresponding charge collected from the midgap injection. Studies on the effect of charge injection induced surface current in non-irradiated strip sensors has been published in references [92, 93].

5.1.2 Charge collection in the p-on-p sensor

The characterization study of the thin p-on-p pixel sensor by TCAD simulations demonstrates their versatility in the investigation of an unknown or less studied device configuration.

The initial charge collection simulations from a backplane injection with carrier lifetimes tuned to reproduce experimentally matching leakage current ratio between the two sensors resulted in a qualitative agreement with measurement but with considerably smaller voltage dependence. The result displayed the prevalent effect of the more favourable weighting field in the p-on-n sensor over the higher electric field at the location of the charge injection in the p-on-p sensor at low voltages.

The voltage dependent charge collection of the p-on-p sensor was possible to tune

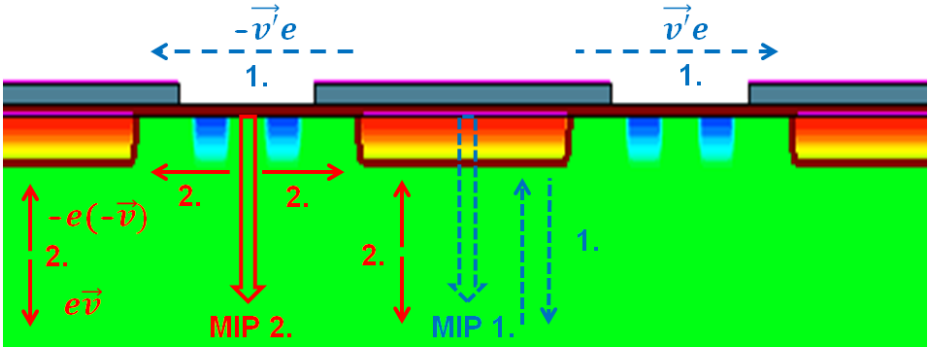

Figure 5.1: A schematic illustration of the induced transient currents in a n-on-p strip sensor from MIP injections at the center of the strip (1.) and at midgap between the strips (2.). The drift vector $\vec{v}'$ along the sensor surface is perpendicular to the drift vectors between the anode and cathode resulting in an opposite sign contribution to the cluster charge collected in the sensor.

close to the measured behaviour by further decreasing the charge carrier lifetimes. This effective approach showed that the lower charge collection at low voltages in the p-on-p sensor could be explained by the higher hole trapping in the p-bulk. Combined with the measured lower leakage current in the p-on-p sensor this suggests the presence of deep level traps in the p-bulk with significant hole trapping probability and a small contribution to the leakage current [35]. To maintain the experimentally agreeing leakage current levels, further tuning of the simulated charge collection should include such traps.

5.1.3 Deep donors in the GaAs epi-layer

The DLTS analysis of the GaAs X-ray detectors revealed a significant concentration of deep level electron traps in the epitaxial layer. When these were modeled in the TCAD simulations with a deep donor defect level the measured leakage current density and V_{fd} were reproduced. Compared to the preliminary estimation from the DLTS measurements, the three orders higher effective capture cross section of the tuned donor level needed for the simulation could be interpreted as an indication of another deeper level not seen in the investigated DLTS temperature range. That is, if only one defect level is implemented in the simulation, a higher concentration and cross section values are required to compensate the absence of the possible additional deep level in the real GaAs epi-layer.

5.2 Practical implications

Improvement in the accuracy of the defect model to reproduce measured results will inevitably also lead to increased predictive power. The ability to make reliable predictions of detector performance evolution with accumulating fluence is an essential element in the R&D of radiation hard detectors. The Sentaurus TCAD defect model presented in the course of this thesis produces a comprehensive set of measurement-calibrated detector properties (V_{fd}, I_{leak}, E(depth), CCE, R_{int}, CCE(x), C_{int}) in both surface and bulk that govern the charge collection and resolution of a strip detector irradiated to HL-LHC fluences.

The electric field distributions in the thin p-on-p pixel sensor show that, after full depletion is reached, the field maximum is at the pixel edges, due to geometrical effect seen on all segmented devices. Since the pn-junction in the p-on-p device is at the non-segmented side, the electric field peaks at the pixels and the backplane lead to a low full depletion voltage of the bulk. When the pn-junction is at the pixel side as in the p-on-n sensor, the resulting V_{fd} is higher than in a non-segmented device due to the lateral expansion of the electric field that slows the extension towards the backplane.

The interpixel resistance simulations in the two sensor types displayed identical behaviour after full depletion. Also, the difference in the simulated breakdown voltages of the two sensors was negligible. Hence, the location of the pn-junction at the non-segmented side in the p-on-p detector does not result in any significant advantage in this regard.

Thus, the measurements and the simulation study of the thin p-on-p pixel detector displayed equal electrical and charge collection performance to the more typical p-on-n active edge pixel detector at voltages above ∼80 V. Since the sensors at the LHC experiments are operated at over-depleted mode to maximize the carrier velocities, the p-on-p sensors could offer a cost effective alternative to the current p-on-n sensors at the outer layers with lower fluences in the foreseen upgrades without compromising charge collection properties or resolution while providing more stable operation due to the absence of the type inversion.

The close reproduction of the C-V/I-V and TCT measurements of the epitaxial GaAs pin-diode radiation detectors by TCAD simulations displayed that the effective semiconductor device modeling can be extended beyond silicon material. The possibility to tune the properties of the modeled GaAs device by inserting experimentally observed microscopic defects to the simulation as well as the ability to reproduce the transient

signal behavior characteristic to GaAs has a potential for high accuracy studies. This could be exploited *en masse* in the field for accelerated and cost effective R&D of the GaAs radiation detectors.

5.3 Reliability and validity

The baseline for all simulations conducted in the course of this research was to validate the results at every step with respect to experimental data.

Detailed simulations with non-irradiated sensors and diodes have proven that the implemented device design can reproduce the observed measurement results. Charge carrier lifetimes and doping profiles of the simulation devices have been iterated and adapted in the studies conducted by the CMS Device Simulations workgroup [57, 88]. This can be considered as a basic requirement before radiation-induced defects can be implemented to the simulation.

Simulation results obtained by the Silvaco Atlas and Synopsys Sentaurus TCAD defect models for bulk and surface damage have also been cross-checked whenever possible. So far it has been established that both approaches, N_{it} confined to the Si/SiO_2 interface and having a wider depth distribution, provide the expected strip isolation as well as similar electric field profiles between the strips at high proton fluences and hence, at high values of Q_{f}. However, at this time no Silvaco Atlas model produced C_{int} or CCE(x) results have emerged preventing the full comparison and validation of the approaches.

5.4 Recommendations for further research

For more complete modeling of the CCE(x), test beam measured charge collection data of varying pitches of both strip and pixel detectors as well as higher number of fluence points will be required. Future efforts of the defect model developments also include further calibration with the measured edge-TCT data that enables the tuning of the simulated $E(z)$ profile with increased precision.

The ultimate objective of the CCE(Φ) simulations is to stretch the defect models up to $\sim 2 \times 10^{16}$ $\mathrm{n_{eq}cm^{-2}}$ to account for the fluences of the pixel and 3D columnar detectors positioned closest to the vertex at the HL-LHC.

Furthermore, an effort should be made to find a way to tune the standard parameter sets of the Synopsys Sentaurus and Silvaco Atlas packages to produce converging results

of the basic sensor properties. This would lead to a more complete understanding and control over the simulation process.

Even though the 3D-structures are the way to accurately model a real device, the time budget and CPU memory requirements are substantial compared to the 2D-simulations. The parallelization option in the Sentaurus framework enables the distribution of the computing tasks within one node between the available processors in the system. In a typical parameter scan the number of nodes in the simulation can be 10–20 while the simulation of a single node for a 3D-structure as in figure 4.4a can take several days in a standard 32 GB tabletop. Therefore, the grid computing option, where the different nodes would be distributed between several PCs, should be investigated for the effective parameter space study of the pixel and 3D columnar detectors.

Appendices

Appendix A

Simulation process in Sentaurus TCAD

The Synopsys Sentaurus simulation framework utilizes the standard finite element analysis (FEA) scheme of creating a mesh-like grid structure and then solving equations at each mesh point to calculate physical properties.

The equations include Poisson's equation, the current continuity equation and the energy-balance equation for holes and electrons. The recombination and generation models implemented in the packages use concentration and lifetime dependent Shockley-Read-Hall (SRH), Auger and radiative recombination models, as well as concentration and field dependent mobility models. The simulation packages enable the additional generation of charge carriers via the impact ionization, as described by van Overstraeten–de Man [94]. These models are used directly in the solution of the device equation in a self-consistent manner.

Calculations are performed through a discretization process that yields the relationship between variables defined at triangular-shaped grid points. High solution accuracy requires a fine grid that resolves the structure, whereas numerical efficiency is greater when fewer grid points are used. Specifying an optimal grid is an essential part of the device simulation and typically there is a trade-off between the requirements of accuracy and numerical efficiency.

These techniques solve non-linear algebraic systems using an iterative procedure that refines successive estimates of the solution. The non-linear iteration procedure starts from an initial guess and the iterations continue until the corrections are small enough to satisfy convergence criteria, or until a specified number of iterations have been completed.

The simulated devices are described within the simulation packages defining different

components, volumes, layers and electrodes reproducing the actual device design, and assigning physical and electrical properties to each component. Reflecting Neumann boundary conditions are imposed at the outer edges of the structure enabling a more detailed mesh-like grid definition in a smaller volume.

At the guard ring electrodes of a microstrip device current boundary conditions are imposed. By enforcing a condition of zero current during the solution of the equations these electrodes are kept floating. The ohmic contacts at the main p^+ or n^+ strip and backside contacts are implemented using Dirichlet boundary conditions. The boundary conditions are described in detail in [57]. An example configuration and a list of physical models used in Synopsys Sentaurus TCAD are given in the Appendix of the reference [57].

References

[1] F. Gianotti, et al., *Physics potential and experimental challenges of the LHC luminosity upgrade*, hep-ph/0204087 (April 2002).

[2] L. Rossi, O. Brüning, *High Luminosity Large Hadron Collider - A description for the European Strategy Preparatory Group*, CERN-ATS-2012-236 (2012).

[3] I. Dawson, *Radiation predictions at the SLHC and irradiation facilities*, ATLAS Tracker Upgrade Workshop, Liverpool, UK, 2006.

[4] *LHC Project Report 626*, in: F. Ruggiero (Ed.), LHC Luminosity and Energy Upgrade: A Feasibility Study, CERN, 2002.
URL `http://cern.ch/lhc-proj-IR-upgrade/`

[5] V. Eremin, E. Verbitskaya, Z. Li, *The origin of double peak electric field distribution in heavily irradiated silicon detectors*, Nucl. Instr. & Meth. A **476** (2002) 556–564. `doi:10.1016/S0168-9002(01)01642-4`.

[6] V. Eremin, E. Verbitskaya, A. Zabrodskii, Z. Li, J. Härkönen, *Avalanche effect in Si heavily irradiated detectors: physical model and perspectives for application*, Nucl. Instr. & Meth. A **658** (2011) 145–151. `doi:10.1016/j.nima.2011.05.002`.

[7] R. Eber, *Investigations of new Sensor Designs and Development of an effective Radiation Damage Model for the Simulation of highly irradiated Silicon Particle Detectors*, Ph.D. thesis, Karlsruhe Institute of Technology (2013).
URL `http://ekp-invenio.physik.uni-karlsruhe.de/record/48328/files/EKP-2014-00012.pdf`

[8] F. Foulon, et al., *A New Technique for the Fabrication of Thin Silicon Radiation Detectors*, IEEE Trans. Nucl. Sci. **46** (3) (1999) 218 – 220. `doi:10.1109/23.775517`.

[9] G. Casse, *Overview of the recent activities of the RD50 collaboration on radiation hardening of semiconductor detectors for the sLHC*, Nucl. Instr. & Meth. A **598** (2009) 54–60. doi:10.1016/j.nima.2008.08.019.

[10] G. Casse, et al., *First results on the charge collection properties of segmented detectors made with p-type bulk silicon*, Nucl. Instr. & Meth. A **487** (2002) 465–470. doi:10.1016/S0168-9002(02)00263-2.

[11] G. Casse, P. P. Allport, A. Watson, *Effects of accelerated annealing on p-type silicon micro-strip detectors after very high doses of proton irradiation*, Nucl. Instr. & Meth. A **568** (2006) 46–50. doi:10.1016/j.nima.2006.05.200.

[12] S. Terzo, A. Macchiolo, R. Nisius, B. Paschen, *Thin n-in-p planar pixel sensors and active edge sensors for the ATLAS upgrade at HL-LHC*, JINST **9** (C12029). doi:10.1088/1748-0221/9/12/C12029.

[13] A. Owens, A. Peacock, *Compound semiconductor radiation detectors*, Nucl. Instr. & Meth. A **531** (1-2) (2004) 18–37. doi:10.1016/j.nima.2004.05.071.

[14] P. Sellin, J.Vaitkus, *New materials for radiation hard semiconductor detectors*, Nucl. Instr. & Meth. A **557** (2) (2006) 479–489. doi:10.1016/j.nima.2005.10.128.

[15] J. G. Ruch, G. S. Kino, *Transport properties of GaAs*, Phys.Rev. **174** (3) (1968) 921–931.
URL http://journals.aps.org/pr/pdf/10.1103/PhysRev.174.921%

[16] A. Dargys, J. Kundrotas, *Handbook on the physical properties of Ge, Si, GaAs and InP*, 1st Edition, Science and Encyclopedia Publ., Vilnius, Lithuania, 1994.

[17] S. M. Sze, *Physics of Semiconductor Devices*, 2nd Edition, John Wiley & Sons, New Jersey, 1981.

[18] G. F. Knoll, *Radiation Detection and Measurement*, 3rd Edition, John Wiley & Sons, New Jersey, 2000.

[19] E. Tuovinen, *Processing of Radiation Hard Particle Detectors on Chochralski Silicon*, Ph.D. thesis, University of Helsinki, Department of Physics (October 2008).

[20] S. M. Sze, *Semiconductor Devices: Physics and Technology*, John Wiley & Sons, New Jersey, 1985.

[21] S. I. Parker, C. J. Kenney, J. Segal, *3D - A proposed new architecture for solid-state radiation detectors*, Nucl. Instr. & Meth. A **395** (1997) 328–343. doi:10.1016/S0168-9002(97)00694-3.

[22] Z. Li, *New BNL 3D-Trench electrode Si detectors for radiation hard detectors for sLHC and for X-ray applications*, Nucl. Instr. & Meth. A **658** (2011) 90–97. doi:10.1016/j.nima.2011.05.003.

[23] A. Montalbano, et al., *A systematic study of BNL's 3D-Trench Electrode detectors*, Nucl. Instr. & Meth. A **765** (2014) 23–28. doi:10.1016/j.nima.2014.03.066.

[24] C. Piemonte, et al., *Development of 3D detectors featuring columnar electrodes of the same doping type*, Nucl. Instr. & Meth. A **541** (2005) 441–448. doi:10.1016/j.nima.2005.01.087.

[25] G. Pellegrini, et al., *First double-sided 3-D detectors fabricated at CNM-IMB*, Nucl. Instr. & Meth. A **592** (2008) 38–43. doi:10.1016/j.nima.2008.03.119.

[26] M. Lundqvist, B. Cederström, V. Chmill, M. Danielsson, B. Hasegawa, *Evaluation of a photon counting X-ray imaging system*, IEEE Trans. Nucl. Sci. **48** (2000) 1530–1536. doi:10.1109/NSSMIC.2000.948998.

[27] M. Prest, et al., *FROST: a low-noise high-rate photon counting ASIC for X-ray applications*, Nucl. Instr. & Meth. A **461** (2001) 435–439. doi:10.1016/S0168-9002(00)01268-7.

[28] *RD50 Status Report 2009/2010–Radiation hard semiconductor devices for very high luminosity colliders*, http://cds.cern.ch/record/1455062/files/LHCC-SR-004.pdf?version=1, CERN-LHCC-2012-010, LHCC-SR-004.

[29] M. Moll, *Development of radiation hard sensors for very high luminosity colliders–CERN-RD50 project*, Nucl. Instr. & Meth. A **511** (2003) 97–105. doi:10.1016/S0168-9002(03)01772-8.

[30] G. Lindström, et al., *Radiation hard silicon detectors–developments by the RD48 (ROSE) collaboration*, Nucl. Instr. & Meth. A **466** (2001) 308–326. doi:10.1016/S0168-9002(01)00560-5.

[31] G. Kramberger, V. Cindro, I. Mandić, M. Mikuž, M. Zavrtanik, *Effective trapping time of electrons and holes in different silicon materials irradiated with neutrons, protons and pions*, Nucl. Instr. & Meth. A **481** (2002) 297–305. doi:10.1016/S0168-9002(01)01263-3.

[32] G. Pellegrini, et al., *Technology development of 3D detectors for high-energy physics and imaging*, Nucl. Instr. & Meth. A **487** (2002) 19–26. doi:10.1016/S0168-9002(02)00939-7.

[33] G. Lindström, *Radiation damage in silicon detectors*, Nucl. Instr. & Meth. A **512** (2003) 30–43. doi:10.1016/S0168-9002(03)01874-6.

[34] M. Moll, *Radiation Damage in Silicon Particle Detectors–microscopic defects and macroscopic properties–*, Ph.D. thesis, University of Hamburg, DESY-THESIS-1999-040 (December 1999).

[35] R. Radu, I. Pintilie, L. C. Nistor, E. Fretwurst, G. Lindström, L. F. Makarenko, *Investigation of point and extended defects in electron irradiated silicon-Dependence on the particle energy*, J. Appl. Phys. **117** (164503). doi:10.1063/1.4918924.

[36] I. Pintilie, E. Fretwurst, G. Lindström, J. Stahl, *Results on defects induced by ^{60}Co gamma irradiation in standard and oxygen-enriched silicon*, Nucl. Instr. & Meth. A **514** (2003) 18–24. doi:10.1016/j.nima.2003.08.079.

[37] I. Pintilie, M. Buda, E. Fretwurst, G. Lindström, J. Stahl, *Stable radiation-induced donor generation and its influence on the radiation tolerance of silicon diodes*, Nucl. Instr. & Meth. A **556** (2006) 197–208. doi:10.1016/j.nima.2005.10.013.

[38] I. Pintilie, G. Lindström, A. Junkes, E. Fretwurst, *Radiation-induced point- and cluster-related defects with strong impact on damage properties of silicon detectors*, Nucl. Instr. & Meth. A **611** (2009) 52–68. doi:10.1016/j.nima.2009.09.065.

[39] E. Fretwurst, F. Hönniger, G. Kramberger, G. Lindström, I. Pintilie, R. Röder, *Radiation damage studies on MCz and standard and oxygen enriched epitaxial silicon devices*, Nucl. Instr. & Meth. A **583** (2007) 58–63. doi:10.1016/j.nima.2007.08.194.

[40] I. Pintilie, E. Fretwurst, G. Lindström, *Cluster related hole traps with enhanced-field-emission - the source for long term annealing in hadron irradiated Si diodes*, Appl. Phys. Lett. **92** (024101). doi:10.1063/1.2832646.

[41] I. Pintilie, E. Fretwurst, G. Lindström, J. Stahl, *Second-order generation of point defects in gamma-irradiated float-zone silicon, an explanation for "type inversion"*, Appl. Phys. Lett. **82** (2169). doi:10.1063/1.1564869.

[42] A. Junkes, D. Eckstein, I. Pintilie, L. F. Makarenko, E. Fretwurst, *Annealing study of a bistable cluster defect*, Nucl. Instr. & Meth. A **612** (2010) 525–529. doi:10.1016/j.nima.2009.08.021.

[43] V. P. Markevich, et al., *Trivacancy and trivacancy-oxygen complexes in silicon: Experiments and ab initio modeling*, Phys. Rev. B **80** (235207). doi:10.1103/PhysRevB.80.235207.

[44] R. M. Fleming, C. H. Seager, D. V. Lang, E. Bielejec, J. M. Campbell, *Defect-driven gain bistability in neutron damaged, silicon bipolar transistors*, Appl. Phys. Lett. **90** (172105). doi:10.1063/1.2731516.

[45] J. Zhang, I. Pintilie, E. Fretwurst, R. Klanner, H. Perrey, J. Schwandt, *Study of radiation damage 240 induced by 12 keV X-rays in MOS structures built on high-resistivity n-type silicon*, J. Synchrotron Rad. **19** (2012) 340–346. doi:10.1107/S0909049512002348.

[46] J. Zhang, E. Fretwurst, R. Klanner, I. Pintilie, J. Schwandt, M. Turcato, *Investigation of X-ray induced radiation damage at the Si-SiO2 interface of silicon sensors for the European XFEL*, JINST **7** (C12012). doi:10.1088/1748-0221/7/12/C12012.

[47] T. Mäenpää, *Performance of different silicon materials for the upgraded CMS tracker*, in: 11th International Conference on Large Scale Applications and Radiation Hardness of Semiconductor Detectors, Vol. (RD13)**015**, PoS, 2013.
URL http://pos.sissa.it/cgi-bin/reader/contribution.cgi?id%=PoS%28RD13%29015

[48] A. Nürnberg, *Studies on irradiated silicon sensors for the CMS tracker at the HL-LHC*, Ph.D. thesis, Karlsruhe Institute of Technology, IEKP-KA/2014-04 (2014).
URL http://ekp-invenio.physik.uni-karlsruhe.de/record/4857%6/files/EKP-2014-00087.pdf

[49] Z. Li, et al., *Investigation of the Oxygen-Vacancy (A-Center) Defect Complex Profile in Neutron Irradiated High Resistivity Silicon Junction Particle Detectors*, IEEE Trans. Nucl. Sci **39** (1992) 1730–1738. doi:10.1109/23.211360.

[50] J. L. Lindström, B. G. Svensson, *Oxygen-Related Defects in Silicon*, in: Symposium K–Oxygen, Carbon, Hydrogen and Nitrogen in Crystalline Silicon, Vol. **59** of MRS Proceedings, 1985. doi:10.1557/PROC-59-45.

[51] M. Moll, E. Fretwurst, G. Lindström, *Leakage current of hadron irradiated silicon detectors - material dependence*, Nucl. Instr. & Meth. A **426** (1999) 87–93. doi:10.1016/S0168-9002(98)01475-2.

[52] S. J. Watts, C. D. Via, A. Karpenko, *Macroscopic results for a novel oxygenated silicon material*, Nucl. Instr. & Meth. A **485** (2002) 153–158. doi:10.1016/S0168-9002(02)00547-8.

[53] W. Adam, et al., *Performance of irradiated CVD diamond micro-strip sensors*, Nucl. Instr. & Meth. A **476** (2002) 706–712. doi:10.1016/S0168-9002(01)01671-0.

[54] J. Vaitkus, et al., *Semi-insulating GaN and its evaluation for α particle detection*, Nucl. Instr. & Meth. A **509** (2003) 60–64. doi:10.1016/S0168-9002(03)01550-X.

[55] G. Kramberger, et al., *Superior radiation tolerance of thin epitaxial silicon detectors*, Nucl. Instr. & Meth. A **515** (2003) 665–670. doi:10.1016/j.nima.2003.07.021.

[56] J. Härkönen, et al., *Low-temperature TCT characterization of heavily proton irradiated p-type magnetic Czochralski silicon detectors*, Nucl. Instr. & Meth. A **583** (2007) 71–76. doi:10.1016/j.nima.2007.08.198.

[57] A. Bhardwaj, R. Dalal, R. Eber, T. Eichhorn, K. Lalwani, A. Messineo, T. Peltola, M. Printz, K. Ranjan, *Simulation of Silicon Devices for the CMS Phase II Tracker Upgrade*, Compact Muon Solenoid, CMS DN -2014/016 (2015).

[58] ATLAS collaboration, *ATLAS Insertable B-Layer Technical Design Report*, http://cds.cern.ch/record/1291633/files/ATLAS-TDR-019.pdf?version=2, CERN-LHCC-2010-013 (2010).

[59] J. Lange, et al., *Properties of a radiation-induced charge multiplication region in epitaxial silicon diodes*, Nucl. Instr. & Meth. A **622** (2010) 49–58. doi:10.1016/j.nima.2010.07.036.

[60] G. Casse, et al., *Enhanced efficiency of segmented silicon detectors of different thicknesses after proton irradiations up to* 1×10^{16} n_{eq}/cm^2, Nucl. Instr. & Meth. A **624** (2010) 401–404. doi:10.1016/j.nima.2010.02.134.

[61] M. Koehler, et al., *Comparative measurements of highly irradiated n-in-p and p-in-n 3D silicon strip detectors*, Nucl. Instr. & Meth. A **659** (2011) 272–281. doi:10.1016/j.nima.2011.08.041.

[62] E. Verbitskaya, V. Eremin, A. Zabrodskii, Z. Li, P. Luukka, *Restriction on the gain in collected charge due to carrier avalanche multiplication in heavily irradiated Si strip detectors*, Nucl. Instr. & Meth. A **730** (2013) 66–72. doi:10.1016/j.nima.2013.06.086.

[63] G. Pellegrini, et al., *Technology developments and first measurements of Low Gain Avalanche Detectors (LGAD) for high energy physics applications*, Nucl. Instr. & Meth. A **765** (2014) 12–16. doi:10.1016/j.nima.2014.06.008.

[64] G. Kramberger, *Radiation hardness of Low Gain Amplification Detectors (LGAD)*, presented at the 24th RD50 Workshop (June 2014).

[65] G. Kramberger, *Studies of CNM diodes with gain*, presented at the 22nd RD50 Workshop (June 2013).

[66] H. F.-W. Sadrozinski, et al., *Ultra-fast silicon detectors*, Nucl. Instr. & Meth. A **730** (2013) 226–231. doi:10.1016/j.nima.2013.06.033.

[67] H. F.-W. Sadrozinski, et al., *Sensors for ultra-fast silicon detectors*, Nucl. Instr. & Meth. A **765** (2014) 7–11. doi:10.1016/j.nima.2014.05.006.

[68] F. Lemeilleur, et al., *Study of characteristics of silicon detectors irradiated with 24 GeV/c protons between -20° C and +20° C*, Nucl. Instr. & Meth. A **360** (1995) 438–444. doi:10.1016/0168-9002(94)01728-X.

[69] V. G. Palmieri, K. Borer, S. Janos, C. D. Viá, L. Casagrande, *Evidence for charge collection efficiency recovery in heavily irradiated silicon detectors operated at cryogenic temperatures*, Nucl. Instr. & Meth. A **413** (1998) 475–478. doi:10.1016/S0168-9002(98)00673-1.

[70] B. Dezillie, et al., *Improved Neutron Radiation Hardness for Si detectors: Application of Low Resistivity Starting Material and/or Manipulation of N_{eff} by Selective Filling of Radiation-induced Traps at Low Temperatures*, IEEE Trans. Nucl. Sci. **46** (1999) 221–227. doi:10.1109/23.775518.

[71] V. Eremin, et al., *Current injected detectors (CID)–a new approach for detector operation in very high radiation environment*, IEEE NSS Conf. Rec. **3** (2004) 2003–2006. doi:10.1109/NSSMIC.2004.1462639.

[72] J. Härkönen, et al., *Test beam results of a heavily irradiated Current Injected Detector (CID)*, Nucl. Instr. & Meth. A **612** (2010) 488–492. doi:10.1016/j.nima.2009.08.006.

[73] V. Eremin, et al., *The operation and performance of Current Injected Detector (CID)*, Nucl. Instr. & Meth. A **581** (2007) 356–360. doi:10.1016/j.nima.2007.08.003.

[74] E. Verbitskaya, V. Eremin, Z. Li, J. Härkönen, M. Bruzzi, *Concept of Double Peak electric field distribution in the development of radiation hard silicon detectors*, Nucl. Instr. & Meth. A **583** (2007) 77–86. doi:10.1016/j.nima.2007.08.228.

[75] E. Verbitskaya, V. Eremin, A. Zabrodskii, *Operational voltage of silicon heavily irradiated strip detectors utilizing avalanche multiplication effect*, JINST **7** (C02061). doi:10.1088/1748-0221/7/02/C02061.

[76] E. Verbitskaya, V. Eremin, *Simulation of electric field profile in Si irradiated detectors with a consideration of carrier generation parameters*, presented at 21st RD50 Workshop (2012).

[77] S. Väyrynen, *Irradiation of Silicon Particle Detectors with MeV-Protons*, Ph.D. thesis, University of Helsinki, Department of Physics (May 2010).

[78] G. Kramberger, V. Cindro, I. Mandić, M. Mikuž, M. Milovanović, M. Zavrtanik, K. Žagar, *Investigation of Irradiated Silicon Detectors by Edge-TCT*, IEEE Trans. Nucl. Sci. **57** (2010) 2294–2302. doi:10.1109/TNS.2010.2051957.

[79] B. E. Deal, *Standardized Terminology for Oxide Charges Associated with Thermally Oxidized Silicon*, IEEE Trans. Electron Dev. **27** (1980) 606–608. doi:10.1109/T-ED.1980.19908.

[80] R. Klanner, et al., *Challenges for silicon pixel sensors at the European XFEL*, Nucl. Instr. & Meth. A **730** (2013) 2–7. doi:10.1016/j.nima.2013.05.166.

[81] C. Eklund, et al., *Silicon beam telescope for CMS detector tests*, Nucl. Instr. & Meth. A **430** (1999) 321–332. doi:10.1016/S0168-9002(99)00210-7.

[82] J. Härkönen, et al., *Test beam results of a heavily irradiated Current Injected Detector (CID)*, Nucl. Instr. & Meth. A **612** (2010) 488–492. doi:10.1016/j.nima.2009.08.006.

[83] R. Dalal, A. Bhardwaj, K. Ranjan, K. Lalwani, G. Jain, *Simulation of Irradiated Si Detectors*, in: The 23rd International Workshop on Vertex Detectors, Vol. (Vertex2014)**030**, PoS, 2014.
URL http://pos.sissa.it/cgi-bin/reader/contribution.cgi?id=PoS%28Vertex2014%29030

[84] C. Piemonte, *Device Simulations of Isolation Techniques for Silicon Microstrip Detectors Made on p-Type Substrates*, IEEE Trans. Nucl. Sci. **53** (2006) 1694–1705. doi:10.1109/TNS.2006.872500.

[85] Y. Unno, et al., *Optimization of surface structures in n-in-p silicon sensors using TCAD simulation*, Nucl. Instr. & Meth. A **636** (2011) 118–124. doi:10.1016/j.nima.2010.04.095.

[86] G. Verzellesi, G.-F. D. Betta, G. Pignatel, *Compact modeling of n-side interstrip resistance in p-stop and p-spray isolated double-sided silicon microstrip detectors*, IEEE Nucl. Sci. Symp. **1** (2000) 25–27. doi:10.1109/NSSMIC.2000.949004.

[87] T. Peltola, J. Härkönen, *TCAD simulated surface damage in proton irradiated strip sensors: Investigation of interface traps vs non-uniform 3-level model*, presented at the 25th RD50 Workshop (2014).

[88] T. Eichhorn, A. Bhardwaj, R. Dalal, R. Eber, K. Lalwani, A. Messineo, T. Peltola, M. Printz, K. Ranjan, *Simulations of Inter-Strip Capacitance and Resistance for the Design of the CMS Tracker Upgrade*, in: Technology and Instrumentation in Particle Physics 2014, Vol. (TIPP2014)**279**, PoS, 2014.
URL http://pos.sissa.it/cgi-bin/reader/contribution.cgi?id=PoS%28TIPP2014%29279

[89] J. Kalliopuska, X. Wu, J. Jakubek, S. Eränen, T. Virolainen, *Processing and characterization of edgeless radiation detectors for large area detection*, Nucl. Instr. & Meth. A **731** (2013) 205–209. doi:10.1016/j.nima.2013.06.097.

[90] J. S. Blakemore, *Semiconducting and other major properties of gallium arsenide*, J. Appl. Phys. **53**. doi:10.1063/1.331665.

[91] T. Peltola, V. Eremin, E. Verbitskaya, J. Härkönen, *Signal formation in segmented Si planar detectors: TCAD simulated effect of SiO_2 passivation layer*, presented at the 26th RD50 Workshop (2015).

[92] V. Eremin, J. Bohm, S. Roe, G. Ruggiero, P. Weilhammer, *The charge collection in single side silicon microstrip detectors*, Nucl. Instr. & Meth. A **500** (2003) 121–132. doi:10.1016/S0168-9002(03)00330-9.

[93] E. Verbitskaya, et al., *Effect of SiO_2 Passivating Layer in Segmented Silicon Planar Detectors on the Detector Response*, IEEE Trans. Nucl. Sci. **52** (2005) 1877–1881. doi:10.1109/TNS.2005.856907.

[94] Synopsys Inc., Sentaurus Device User Guide, Version G-2012.06.
URL http://www.synopsys.com